Pressure-to-depth conversion models for metamorphic rocks: derivation and applications

Arthur Bauville[1], **Philippe Yamato**[2,3]

[1]Japan Agency for Marine-Earth Science and Technology, 3173–25, Showa-machi, Kanazawa-ku, Yokohama-city, Kanagawa, 236–0001, Japan
[2]Univ Rennes, CNRS, Géosciences Rennes UMR 6118, Rennes, France
[3]Institut Universitaire de France (IUF), Paris, France

Key Points:

- We present and apply different pressure-to-depth conversion models to a dataset of metamorphic pressure.
- The lithostatic pressure assumption results in an upper estimate of depth at peak pressure (> 100 km).
- A change in stress state < 75 km can trigger a peak to retrograde P decrease and is consistent with the data.

Corresponding author: Arthur Bauville, abauville@jamstec.go.jp

Abstract

Pressure-to-depth conversion is a crucial step towards geodynamic reconstruction but remains strongly debated. Here, we derive pressure-to-depth conversion models using either one or two pressure data points in conjunction. In the two-point method, we assume that both peak and retrograde pressure are recorded at the same depth. This method reduces the depth estimate uncertainty dramatically. We apply the proposed pressure-to-depth conversions to a large set of P data from (ultra)high-pressure metamorphic rocks. We explore different cases to explain the transition from peak to retrograde pressure by varying the direction and magnitude of stress components. Our results show that (1) even small deviatoric stresses have a significant impact on depth estimates, (2) the second principal stress component σ_2 plays an essential role, (3) several models can explain the P evolution of the data but lead to different depth estimates, and (4) strain data offer a means to falsify two-point models. The most commonly used pressure-to-depth conversion method uses one pressure point and the assumption that pressure is lithostatic. Then, the transition from peak to retrograde pressure is interpreted as the result of deep subduction (> 100 km), followed by fast exhumation to mid-crustal depth. We show that alternative models where a change in the stress state at a constant depth triggers the pressure transition explain the data equally well. The predicted depth is then shallower than the crustal root Moho (< 75 km) for all data points.

Plain Language Summary

During the formation of mountain belts, rocks are buried deep in the Earth and then exhumed. In this journey, rocks undergo transformations that record the pressure. We use the pressure to estimate the depth at which a rock was buried to reconstruct the history of mountain belts. The pressure is the sum of the weight of the overlying column of rock and tectonic forces. However, since tectonic forces cannot be measured, there has been a long-standing debate on how much they influence the record of pressure in rocks. Here, we use mathematics and computer code to recalculate the burial depth of a set of rock from pressure data. Two extreme scenarios emerge: (1) when ignoring tectonic forces (classical approach), we interpret the pressure history as the result of deep burial (up to 160 km) followed by fast exhumation ($1-10$ cm/yr) to approximately 20 km. The mechanism of such fast exhumation is itself intensely debated; (2) when considering tectonic forces, an alternative scenario is that the rock was buried to an intermediate depth (< 75 km), followed by a change in tectonic forces without exhumation. If this second scenario is verified, then the current history of mountain belts must be re-evaluated.

1 Introduction

Geodynamic reconstructions presenting cross-sections, maps, or elaborate large-scale plate reconstructions over time are essential to conceptualize lithospheric processes such as subduction or mountain building and to reconstruct Earth's history. These geodynamic reconstructions are based on quantitative data obtained with a wide range of techniques from field mapping to geophysical imaging. Among these data, pressure-temperature-time-deformation ($P-T-t-\epsilon$) paths obtained from petrological, geochronological, and mineral deformation studies constitute key constraints. These features are indeed the only way to estimate the burial, temperature and deformation evolution of a piece of rock and, by extension, of the geological unit to which it belongs. In particular, estimated depths, in conjunction with geochronological data, are used to reconstruct the formation process of orogens (e.g., Chopin, 2003; Ernst et al., 2007; Agard et al., 2009).

The conversion of pressure to depth is crucial in establishing a geodynamic reconstruction based on petrographic data. Depth can be retrieved from the lithostatic pressure P_{litho}, i.e., the weight of the overlying column of rock, by the formula:

$$z = \frac{P_{litho}}{\rho g}, \tag{1}$$

where ρ is the average density of the rock column, g is the gravitational acceleration and z is depth. However, P_{litho} cannot be directly estimated from metamorphic rocks; instead, we can estimate the mean stress, also called the pressure, P (Moulas et al., 2019). Therefore, an additional step is required to relate P to P_{litho}. This additional step involves information about the three-dimensional deviatoric stress state responsible for rock deformation. Unfortunately, deviatoric stresses cannot be measured, and one must, therefore, make assumptions regarding the stress state to retrieve P_{litho}. Depending on the assumption made, the final depth estimate can vary by more than a factor of two. Since these crucial assumptions are hard or maybe impossible to falsify, there has been a long-standing debate over (1) what is the most adequate stress state assumption to use for pressure-to-depth conversion, (2) how deeply were metamorphic rocks buried, and (3) how are metamorphic rocks exhumed (e.g., Jamieson, 1963; Ernst, 1963; Brace et al., 1970; Mancktelow, 1993; Godard, 2001; Green, 2005; Agard et al., 2009; Wheeler, 2014; B. Hobbs & Ord, 2015; Wheeler, 2014; Tajčmanová, 2015; Moulas et al., 2013; Gerya, 2015; B. E. Hobbs & Ord, 2017; Moulas et al., 2019; Schmalholz & Podladchikov, 2014; Yamato & Brun, 2017; Reuber et al., 2016; Schenker et al., 2015).

The most common assumption is to ignore deviatoric stresses because metamorphic rocks are assumed to be weak at the depths considered (e.g., Guillot et al., 2009; Agard et al., 2009; Beltrando et al., 2007; Rubatto et al., 2011). Thus, $P = P_{litho}$ and one can readily use eq. 1. We call this assumption the "lithostatic case". In a rock, the magnitude of deviatoric stresses can vary from zero to the point of rock failure. Hence, the mean deviatoric stress can be of a magnitude comparable to lithostatic pressure, and P can vary from 1 to 2 times the value of P_{litho} in compression for a homogeneous rock (Petrini & Podladchikov, 2000). The difference between P and P_{litho} is referred to as "tectonic pressure" (Mancktelow, 2008), "tectonic overpressure" (Mancktelow, 1993; Schmalholz & Podladchikov, 2013) or simply "overpressure" when it is positive or "underpressure" when it is negative (Moulas et al., 2013). Note that the overpressure model is a general model of which the "lithostatic case" constitutes one special case. Therefore, it is essential to consider variations in the stress state when interpreting pressure-temperature ($P - T$) paths.

In most cases, the $P - T$ evolution of a (U)HP metamorphic rock can be approximated by three linear segments. A prograde segment (highlighted in blue in Fig. 1A) that shows increases in both P and T and a retrograde part (in green in Fig. 1A) divided in two segments: a retrograde *stage 1* and a retrograde *stage 2* (see Fig. 1A). The first stage of the retrograde path generally shows a large decrease in pressure and only minor variations in temperature, while the second stage presents decreases in both pressure and temperature conditions (?, ?, see)]Yamato2017. Hereafter, we use the notations P_p and T_p to refer to the pressure and temperature conditions at the peak of (U)HP metamorphism (time t_1 in Fig. 1A), respectively. Similarly, P_r and T_r refer to the pressure and temperature conditions at the end of retrograde *stage 1* (time t_2 in Fig. 1A).

There are arguably two events in the $P - T$ path that cause most of the debate: peak metamorphism (P_p, T_p) and retrograde *stage 1* (i.e., the transition from P_p to P_r). Thermobarometric studies often provide P_p, T_p and P_r, T_r, sometimes in association with geochronological dating. We present the dataset of P_p, T_r-P_r, T_r collected from the literature in the $P - T$ space in Figure 1B and in the space P_p-P_r in Figure 1C. In P_p-P_r space, most data points are contained within a fan centered on 0, which suggests that P_p and P_r are proportional, with coefficients of proportionality, P_p/P_r, between 2.4 and 4.8. A few data points with values $P_p < 1.5$ have a coefficient of proportionality < 2.4 as low as 1.4. We term these points "Others (outliers)".

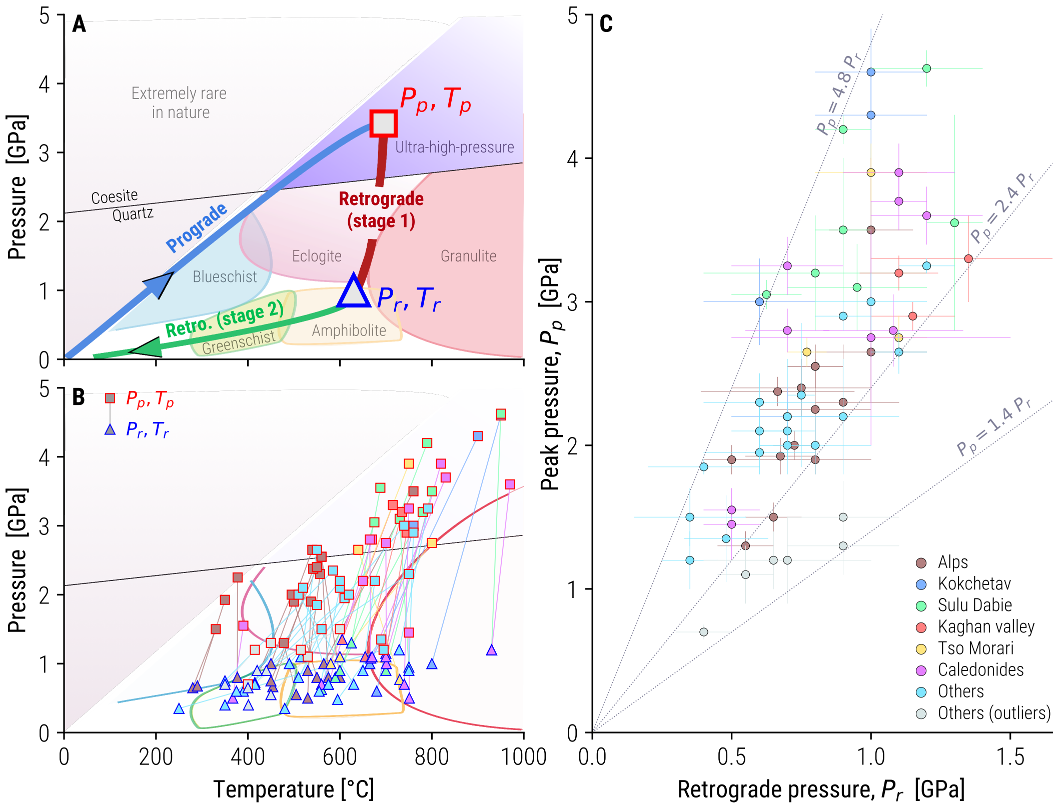

Figure 1. (A) Typical example of a $P - T$ path. (B) Dataset in $P - T$ space. Colors correspond to the orogenic system from which data come as presented in C. (C) Repartition of the data (see Suppl. Mat. for references) in a P_p vs. P_r diagram

To illustrate the consequence of stress state assumptions on geodynamic interpretations, let us consider a rock presenting a mineral paragenesis equilibrated at 3.0 GPa. This rock can be interpreted as having been buried up to 100 km depth under the "lithostatic" assumption (using $\rho = 3000\ kg/m^3$ and $g = 10\ m/s^2$) but only approximately 50 km when considering a magnitude of deviatoric stresses close to the brittle yield stress in compression. While the former corresponds to mid-lithospheric depth, the latter would correspond to crustal-root depth. Pleuger and Podladchikov (2014), for example, proposed a geodynamic reconstruction of the central Alps based on structural arguments wherein the Adula nappe, an eclogite-bearing metamorphic unit in the Alps, was buried to 50-60 km depth. This depth estimate implies an overpressure of 40-80 % of the lithostatic pressure and suggests that the burial and exhumation of this unit occurred within an orogenic crustal wedge. In alternative models using the "lithostatic assumption", the nappe was buried to 80 km depth during subduction and then rapidly exhumed by slab breakoff (S. M. Schmid et al., 1996; Froitzheim et al., 2003) or subvertical extreme thinning (Nagel, 2008). The scenario of S. M. Schmid et al. (1996) employs one subduction zone in conjunction with a normal fault, while the models of (Froitzheim et al., 2003) and Nagel (2008) involve two subduction zones. Thus, different assumptions regarding pressure-to-depth conversion lead to different interpretations of the process of mountain building. Therefore, it is crucial to understand, compare, and evaluate the implications of different assumptions about the stress state when designing geodynamic reconstructions.

Retrograde *stage 1*, when the pressure decreases from P_p to P_r in a relatively short amount of time, is also at the center of heated debate. Using the "lithostatic assumption", the transition from P_p to P_r is interpreted as an exhumation event. In conjunction with dating data, this phase of exhumation is generally interpreted as fast, with exhumation rates comparable to subduction rates (1-10 cm/yr) (e.g., Rubatto & Hermann, 2001; Parrish et al., 2006). Various mechanisms have been proposed to explain these fast exhumation rates, such as buoyancy-driven exhumation (Wheeler, 1991; Beaumont et al., 2009; Butler et al., 2013, 2014; E. Burov et al., 2014; Schmalholz & Schenker, 2016), slab breakoff (Huw Davies & von Blanckenburg, 1995), normal faulting (Platt, 1986; Ring et al., 1999; S. M. Schmid et al., 1996), rollback (Brun & Faccenna, 2008), or channel flow (e.g., Guillot et al., 2009). These and other mechanisms are discussed in detail in several reviews (Guillot et al., 2009; B. R. Hacker & Gerya, 2013; Warren, 2013). In contrast to the fast exhumation interpretation, Yamato and Brun (2017) showed that when considering the large deviatoric stresses assumption, the transition from P_p to P_r can be explained, for many rock samples, by a switch from a compressional to an extensional stress state without exhumation.

In this contribution, we first review the mathematical background of pressure and stress. Then, we formulate a "one-point method" of pressure-to-depth conversion to estimate depth based on a single pressure data point and a "two-point method" that uses both P_p and P_r with the assumption that $z_p = z_r$. We apply these methods to our dataset (Fig. 1B) to determine an estimated depth range for each sample. Finally, we discuss the consequences of different assumptions for geodynamic interpretation and point out ways of falsifying some assumptions. Our goal is both to raise awareness about the issue of pressure-to-depth conversion and to provide tools allowing one to perform such conversion easily. For this reason, we provide computer codes (Jupyter notebooks) as supplementary information S2-S10. These scripts allow readers to reproduce most of the figures presented in this article readily and to extend the database with their own data. The codes can also be used to experiment with stress states and material properties.

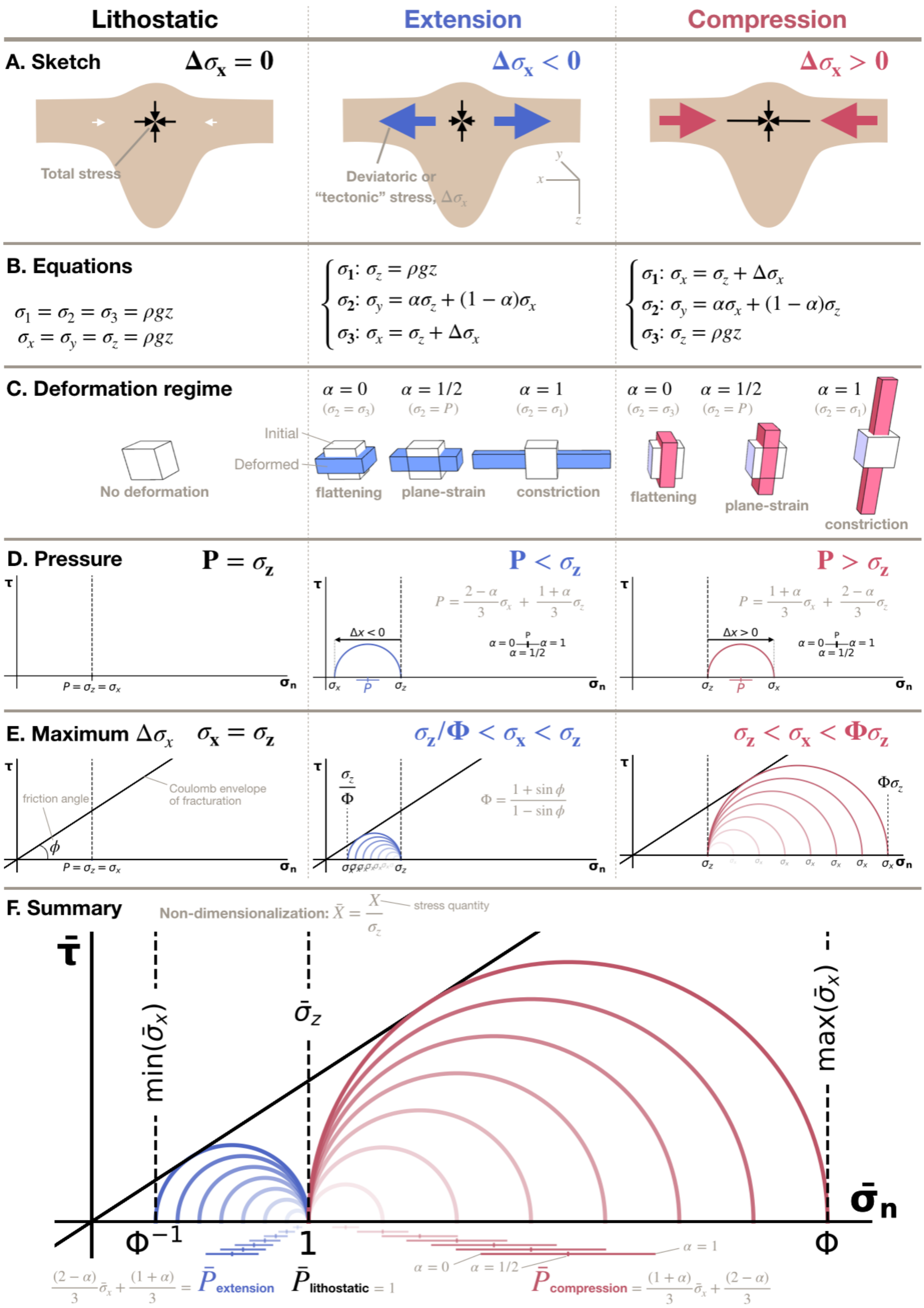

Figure 2. Overview of the principal characteristics of the model and definitions. See text for details concerning notation. $\Delta\sigma_x$ corresponds to the stress magnitude applied in the x-direction. Graphics presenting σ_n vs. τ (i.e., normal stress vs. shear stress) correspond to Mohr diagrams.

2 One-point method of pressure-to-depth conversion

2.1 Overview of the model

2.1.1 Sketch, coordinate system and equations of stress

Let us consider an ideal and simplified orogen submitted to horizontal tectonic stresses in a three-dimensional Cartesian orthonormal system (x, y, z) where z is vertical and points downward and x is the direction in which tectonic loading is applied (Fig. 2A). $\sigma_x, \sigma_y, \sigma_z$ are the normal components of the stress tensor in this coordinate system, and $\sigma_1, \sigma_2, \sigma_3$ are the principal stresses. We use the convention that stresses are positive in compression. We assume, in a first step, that the stress state is Andersonian, that is, one principal stress direction is vertical, and the other two are horizontal (Anderson, 1905). We fix the y-axis in the direction of σ_2. Thus, we only consider cases where the stress state can induce normal or reverse faulting, and we ignore the stress states that would result in strike-slip faulting. Under these assumptions, the total vertical stress σ_z corresponds to the weight of the column of rock above the considered point (or P_{litho}) and is given by:

$$\sigma_z = \rho g z, \tag{2}$$

where ρ is the density of the overlying rocks, g is the gravitational acceleration and z is the depth where the computation is performed. When a tectonic stress of magnitude $\Delta\sigma_x$ is applied in the x-direction, the following equation applies:

$$\sigma_x = \sigma_z + \Delta\sigma_x \tag{3}$$

Three tectonic regimes can be considered depending on the horizontal loading condition (Fig. 2A): (1) lithostatic, when $\Delta\sigma_x = 0$; (2) compression, when $\Delta\sigma_x > 0$; (3) extension, when $\Delta\sigma_x < 0$. Equations describing the stress state for these three tectonic regimes are presented in Figure 2B.

2.1.2 Deformation

The magnitude of the deformation is proportional to $\Delta\sigma_x$, and the direction of maximum stretch is parallel to the direction of σ_3. Thus, there is no deformation in the lithostatic case, and the maximum stretch is horizontal in the extensional case and vertical in the compressional case. The total stress in the y-direction is always $\sigma_y = \sigma_2$, and we use the variable α that ranges between 0 and 1 to describe σ_2 as a function of σ_1 and σ_3 such that:

$$\sigma_2 = \alpha\sigma_1 + (1 - \alpha)\sigma_3. \tag{4}$$

Figure 2C shows how α is related to the mode of deformation. When $\alpha = 0$, $\sigma_2 = \sigma_3$ (see eq. 4), and the rock deforms by flattening. When $\alpha = 1$, $\sigma_2 = \sigma_1$, and the rock deforms by constriction. When $\alpha = 0.5$, $\sigma_2 = (\sigma_1 + \sigma_3)/2 = P$, and the deformation is plane strain.

2.1.3 Pressure

By definition, pressure (P) corresponds to the isotropic part of the stress tensor and, in principal stress coordinates, it can be expressed as follows:

$$P = \frac{\sigma_1 + \sigma_2 + \sigma_3}{3}. \tag{5}$$

Hence, $P = \sigma_z$ in the lithostatic case, $P < \sigma_z$ in extension (because $\Delta\sigma_x < 0$), and $P > \sigma_z$ in compression (because $\Delta\sigma_x > 0$). The Mohr diagrams in Figure 2D illustrate these relationships. In the diagrams, the horizontal and vertical axes represent the normal stress σ_n and shear stress τ on planes within the rock mass, respectively. Pressure is represented by a cross symbol, where the central vertical bar represents the value of pressure when the rock deforms under plane-strain conditions ($\alpha = 1/2$) and the horizontal bar represents the range of pressure associated with values of α between 0 (flattening) and 1 (constriction). The equation for P as a function of α is obtained by substituting eq. (4) into eq. (5), which yields

$$P = \frac{(1+\alpha)}{3}\sigma_1 \; + \; \frac{(2-\alpha)}{3}\sigma_3. \tag{6}$$

2.1.4 Limit of stress and rock failure

When tectonic loading is applied, rocks first undergo elastic or viscous deformation. Stress loading can be increased up to the point where the rock breaks. At this point, the maximum stresses on a given plane within the rock are given by the Mohr-Coulomb law as:

$$\tau = \tan\phi\sigma_n, \tag{7}$$

where ϕ is the friction angle. Rock experiments show that $\phi \approx 30°$ for most rock types (Byerlee, 1978). To simplify the derivation, we ignore cohesion since it is small (order of $10 - 50$ MPa) compared to the pressure of metamorphic rocks considered here (order of GPa). The supplementary scripts (supplementary information S2 to S10) also allow the reader to reproduce most figures in this publication while taking cohesion into account (see Yamato and Brun (2017) for the derivation). Mohr's circle is defined by

$$\sigma_n = \frac{\sigma_1 + \sigma_3}{2} - \frac{\sigma_1 - \sigma_3}{2}\sin\phi \tag{8}$$

and

$$\tau = \frac{\sigma_1 - \sigma_3}{2}\cos\phi. \tag{9}$$

Substituting eq. (8) and eq. (9) into eq. (7) yields

$$\sigma_1 = \Phi\sigma_3, \text{ with} \tag{10}$$

$$\Phi = \frac{1+\sin\phi}{1-\sin\phi}. \tag{11}$$

Figure 2E illustrates the possible stress states associated with different tectonic regimes. This figure presents the whole range of possibilities from the "lithostatic" case to the brittle case.

In extension, $\sigma_x = \sigma_3$, and $\sigma_z = \sigma_1$; therefore, the minimum total horizontal stress is $min(\sigma_x) = \sigma_z/\Phi$ (Fig. 2E, middle panel). Conversely, in compression, $\sigma_x = \sigma_1$, and $\sigma_z = \sigma_3$; therefore, the maximum total horizontal stress is $max(\sigma_x) = \Phi\sigma_z$ (Fig. 2E, right panel). The quantity $(\sigma_1 - \sigma_3)/2$, i.e., the radius of the Mohr circle, is also called the second invariant of the deviatoric stress tensor or the "magnitude of deviatoric stresses".

2.1.5 Summary

Finally, Figure 2F presents a Mohr-Coulomb diagram that summarizes the discussion to this point. The diagram is presented in a non-dimensional form where the overbar indicates that a quantity is normalized by σ_z (e.g., $\bar{\sigma}_x = \sigma_x/\sigma_z$). The pressure in the lithostatic case, or lithostatic pressure, is equal to σ_z (i.e., the weight of the column of rocks). The nondimensional lithostatic pressure is therefore equal to $\bar{\sigma}_z = 1$ (Fig. 2F). In compression, the normalized total horizontal stress $\bar{\sigma}_x$ can vary from 1 (no deformation) to Φ (onset of brittle deformation), and $P > \sigma_z$. In extension, $\bar{\sigma}_x$ can vary from $1/\Phi$ (brittle deformation) to 1 (no deformation), and $P < \sigma_z$. In these three cases, following eq. (5), the nondimensional pressure $\bar{P}$ can then be written as:

$$\bar{P}_l = 1, \tag{12}$$

$$\bar{P}_e = \frac{2-\alpha}{3}\bar{\sigma}_x + \frac{1+\alpha}{3}, \tag{13}$$

$$\bar{P}_c = \frac{1+\alpha}{3}\bar{\sigma}_x + \frac{2-\alpha}{3}, \tag{14}$$

where the subscripts c, e, and l relate to the compression, extension and lithostatic tectonic regimes, respectively (see also Fig. 2F). Another useful result is obtained by solving the previous equations for σ_z:

$$\begin{cases} \sigma_z = \dfrac{3P}{1+\alpha+\bar{\sigma}_x(2-\alpha)}, \text{ when } \bar{\sigma}_x \leq 0, \\ \sigma_z = \dfrac{3P}{2-\alpha+\bar{\sigma}_x(1+\alpha)}, \text{ when } \bar{\sigma}_x \geq 0. \end{cases} \tag{15}$$

2.2 Pressure-to-depth conversion ratio z/P

To convert metamorphic pressure estimates (P) into depth (z), one can use the simple relation $z = \frac{z}{P}P$, where z/P is the gradient of depth as a function of pressure, which we refer hereafter as the "pressure-to-depth conversion ratio", expressed in km/GPa, and is equal to

$$\frac{z}{P} = \frac{1}{\rho g\ \bar{P}}, \text{where} \tag{16}$$

$$\bar{P} = P/\sigma_z. \tag{17}$$

Figure 3 shows graphs of $1/\bar{P}$ and z/P as a function of the horizontal stresses expressed by $\bar{\sigma}_x$ (horizontal axis) and α (different lines). The graphs were calculated by substituting $\bar{P}$ in eq. (16) with eq. (13) when $\bar{\sigma}_x \leq 1$ (i.e., in extension) or eq. (14) when $\bar{\sigma}_x \geq 1$ (i.e., Panels A to E show Mohr diagrams illustrating the stress state for given values of $\bar{\sigma}_x$). Throughout this article, we use $\rho g = 28000\ kg/m^2/s^2$, representing crustal rocks. A value of $\tan(\phi) = 0.6$ is often used in the literature. This value is the result of fitting data from rock friction experiments by Byerlee (1978). In the main article, we use the value $\tan(\phi) = 0.65$ that offers a better fit to the data in the absence of cohesion. The difference has only a negligible influence on pressure estimates. Readers can easily recompute our results using any value of cohesion, ϕ, or ρ by using the scripts provided in the supplementary material (supplementary information S2 to S10).

When the pressure is considered lithostatic ($\bar{\sigma}_x = 1$, Fig. 3C), the pressure-to-depth conversion ratio is $z/P = 35\ km/GPa$. However, this ratio varies significantly when $\bar{\sigma}_x$ increases (compression) or decreases (extension). For example, in the case where $\sigma_2 = \sigma_1$ and $\bar{\sigma}_x$ is minimum, $z/P = 64\ km/GPa$ (Fig. 3A). In contrast, when $\bar{\sigma}_x$ is maximum, $z/P = 16\ km/GPa$ (Fig. 3E). Small deviations of $\bar{\sigma}_x$ from 1 have significant impacts on the pressure-to-depth conversion ratio. For example, when the applied tectonic stress $\Delta\bar{\sigma}_x = min(\Delta\bar{\sigma}_x)/4$, $z/P = 39\ km/GPa$ (Fig. 3B), and when $\Delta\bar{\sigma}_x = max(\Delta\bar{\sigma}_x)/4$, $z/P = 25\ km/GPa$ (Fig. 3D). The value of α also exerts a strong control on the pressure-to-depth conversion ratio, particularly in extension; e.g., when $\bar{\sigma}_x = \Phi^{-1}$, the conversion ratio varies from 45 to 64 km/GPa depending on the value of α.

2.3 Application of the one-point method

We now apply the pressure-to-depth conversion ratio derived in the previous section to our dataset of peak (P_p) and retrograde (P_r) metamorphic pressures. Figure 4 shows the depths estimated from this conversion. Depth estimates at peak pressure (z_p)

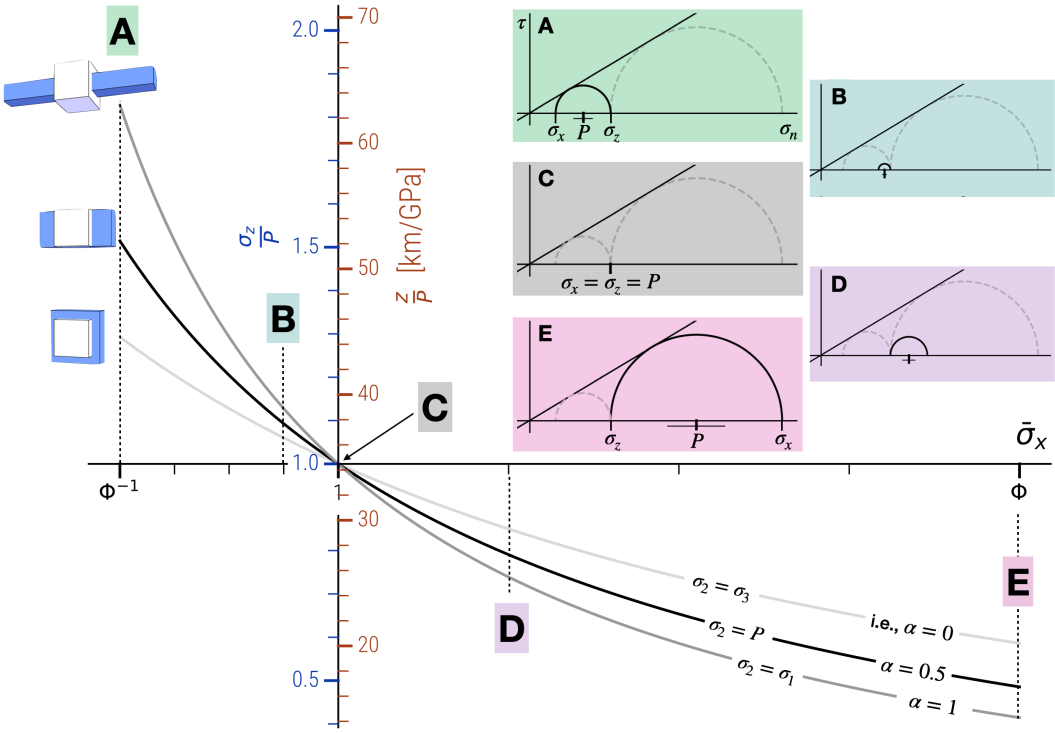

Figure 3. Pressure-to-depth conversion ratio (z/P) as a function of normalized horizontal stress $\bar{\sigma}_x = \sigma_x/\sigma_z$. The vertical axis indicates the ratio of vertical stress to pressure (Sz/P, blue axis) or the pressure-to-depth conversion ratio (z/P, red). We use $\rho g = 28000\ kg/m^2/s^2$, and $\tan\phi = 0.65$. The three lines correspond to different values of α (i.e. σ_2). The mode of deformation associated with α is illustrated by the cartoons on the left, where the white and blue boxes represent the undeformed and deformed states, respectively. The Mohr diagrams represent the outer envelope of stress states at points A to E. In these panels, pressure P is represented by a cross, as in figure **??**F.

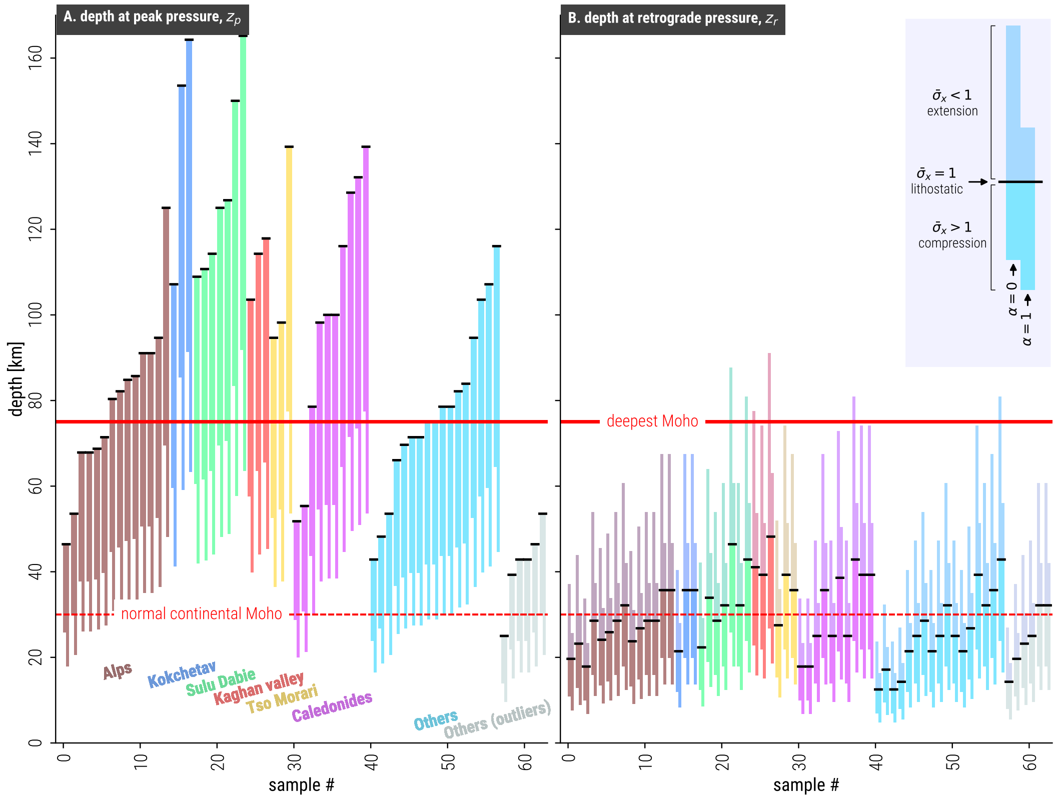

Figure 4. Depth estimates at peak pressure (A) and at retrograde pressure (B) for all samples in our dataset. Colors are coded for areas. The "normal Moho" depth corresponds to the average depth of the continental Moho in regions where the crust is neither thickened nor thinned and is 30 km. The deepest Moho (75 km) corresponds to the current depth of the Moho below the Tibetan Plateau. This figure can be reproduced using the computer script from supplementary information S4.

are shown only for compressive stress states (Fig. 4A), while depth estimates at retrograde pressure (z_r) are shown for both compressive and extensional stress states (Fig. 4B). We indicate two reference depths: (a) 30 km (red dashed line), which is the depth of a "normal continental Moho" defined as the thickness of an isostatically balanced continental crust with topography at sea level, and (b) 75 km (thick red line), which is the depth of the Moho below the Tibetan Plateau and is the present-day "deepest Moho" on Earth. For each sample, the black horizontal bar indicates the lithostatic pressure case. The two columns for each sample indicate the two extreme deformation regimes: flattening ($\alpha = 0$, or $\sigma_2 = \sigma_3$) and constriction ($\alpha = 1$, or $\sigma_2 = \sigma_1$).

At peak pressure conditions, the upper estimate of depth z_p (Fig. 4A, black bars) corresponds to lithostatic conditions (i.e., with no deformation), with a conversion ratio $z/P = 35km/GPa$ (Fig. 4A and Fig. 3C). Under this condition, z_p values are approximately 165 km for samples from the Kokchetav and Sulu-Dabie regions, 140 km for the Tso Morari and Caledonides, and 120 km for the Alps and Kaghan valley. The minimum estimate of z_p results from assuming constricting deformation at brittle failure under compression (i.e., $\alpha = 1$ and $\bar{\sigma}_x = \Phi$). The conversion ratio is then $z/P = 16km/GPa$ (Fig.3E) and $z_p < 75km$ for all samples, i.e., shallower than the present-day deepest Moho on Earth. The uncertainty range for z_p for a single data point varies from ≈15 km for sample #40 to ≈100 km for samples #16 and #23.

Under retrograde conditions, the lithostatic case represents an intermediate estimate because we consider both compressive and extensive tectonic regimes (Fig. 4B). The upper estimate for z_r results from assuming flattening deformation at brittle failure in extension (i.e., $\alpha = 0$ and $\bar{\sigma}_x = 1/\Phi$). The conversion ratio is then $z/P = 64km/GPa$ (Fig. 3A). A few samples from the Alps have a maximum depth estimate of $z_r > 85$ km. For samples from the Kokchetav and Sulu-Dabie orogens, $z_r = 75$ km, and $z_r = 50$ km for samples from the Kaghan valley, Tso Morari and Caledonides. The minimum estimate of z_r results from assuming constricting deformation at brittle failure in compression (i.e., $\alpha = 1$ and $\bar{\sigma}_x = \Phi$). z_r can be as shallow as 10 to 20 km for all samples. The uncertainty range on the estimate of z_r for a single data point is up to 70 km for sample #11 whose maximum depth is ≈ 90 km. All samples have at least part of their range shallower than the deepest present-day Moho at both peak and retrograde pressures.

Figure 5A shows the estimated exhumation calculated as the difference between z_p and z_r. We present six special cases involving different values of $\bar{\sigma}_x^p, \bar{\sigma}_x^r, \alpha_r$, and α_r to illustrate the dependence of the estimated exhumation on the stress state. In Figure 5(C-H), we present Mohr diagrams for these six cases calculated using P_p and P_r from a reference sample.

The maximum exhumation is predicted when P_p corresponds to lithostatic pressure and P_r is recorded at brittle failure in compression (Fig. 5A, top of color bars, and Fig. 5C). The maximum predicted exhumation in our dataset varies between 20 and 150 km.

We use the term "always lithostatic" for the case where both P_p and P_r are lithostatic pressures. This case is shown with black horizontal bars in Figure 5A-B and illustrated in Figure 5D. In this case, exhumation varies between 25 km and 125 km for our dataset. Since the "always lithostatic" case is the most commonly used solution in the literature, we use it as a reference to normalize the results. The normalized graph (Fig. 5B) allows us to express the exhumation amount as a percentage of a reference case and outline similarities between samples.

The red rectangle symbol (Fig. 5A-B) corresponds to a case where deformation is compressive for P_p and extensive for P_r, the magnitude of deviatoric stress is a quarter of the maximum value, and deformation is plane strain (Fig. 5E). This stress state rep-

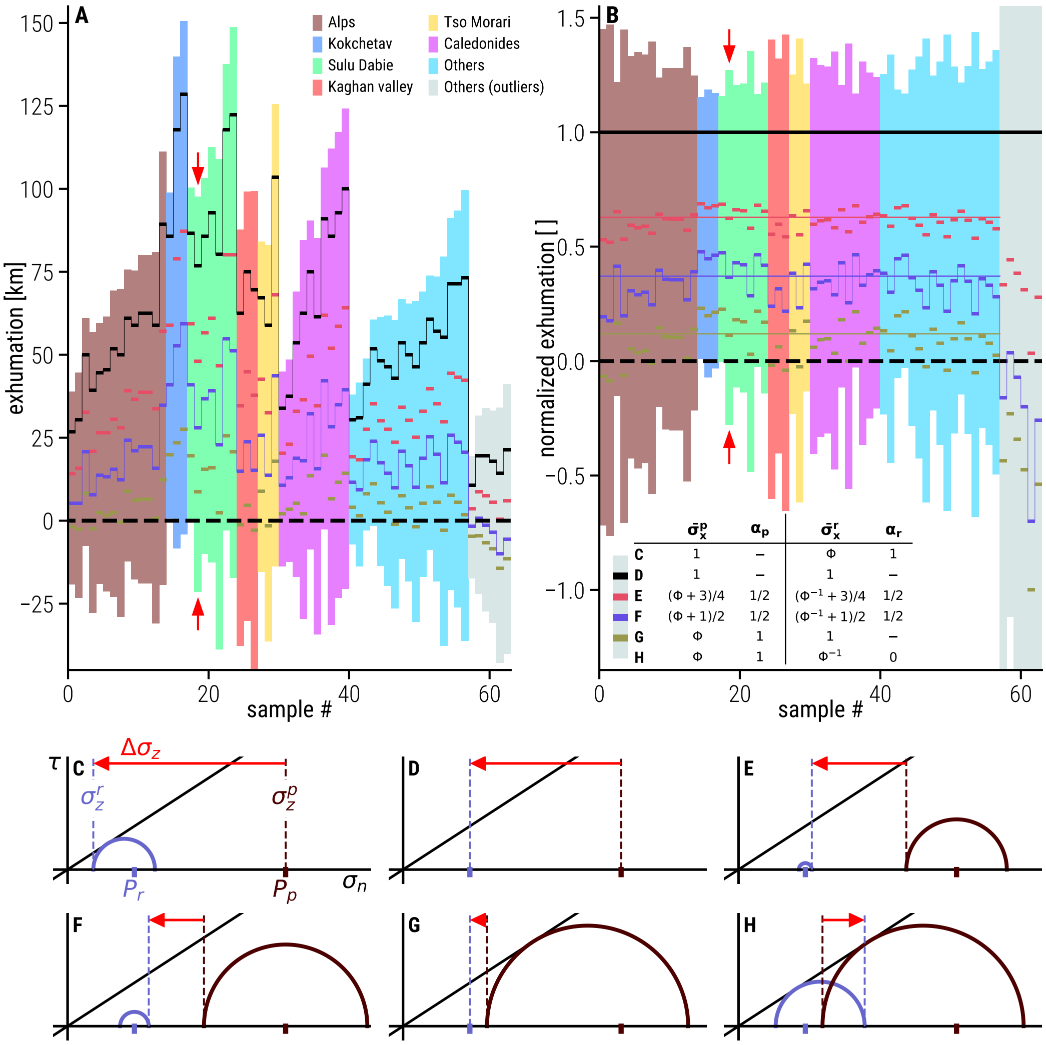

Figure 5. (A) Estimated amount of exhumation calculated as the difference between the estimated depth at peak and retrograde pressures ($z_p - z_r$) for all samples from our dataset. Bar colors indicate the provenance. (B) Same as (A) but normalized by the amount of exhumation obtained by considering P_p and P_r as lithostatic pressures (i.e., "always lithostatic" case). We calculated six special cases by combining different values of $\bar{\sigma}_x^p, \bar{\sigma}_x^r, \alpha_p, \alpha_r$, i.e., maximum and minimum exhumation, and four intermediate cases (colored rectangles). The values used are shown in the table inset in (B). (C-H) Mohr diagrams for the six special cases using P_p, P_r from a reference sample indicated by red arrows in (A) and (B). The characteristics of the special cases are (C) maximum exhumation case, (D) "always lithostatic" case, (E-F) cases with moderate deviatoric stress, (G) exhumation amount close to zero, and (H) minimum exhumation (negative exhumation, i.e., burial). This figure can be reproduced using the computer script from supplementary information S5.

resents a conservative estimate for rocks that deform by viscous deformation at depth. This low deviatoric stress has a significant impact on the quantity of exhumation: on average, this case results in an estimate of exhumation that is only 60% of that for the "always lithostatic" case (see red line in Fig. 5B). The blue rectangle symbol (Fig. 5A-B) represents a case of intermediate stress where the magnitude of deviatoric stress is half of the maximum value (Fig. 5F). On average, this case's results are 35% of the estimate for the "always lithostatic" case (see red line in Fig. 5B). The dark yellow rectangles indicate the scenario where deformation is brittle in compression at peak pressure, and P_r corresponds to lithostatic pressure under plane strain deformation. This scenario predicts at most 30 km of exhumation and a minimum of -10 km (i.e., 10 km of additional burial). In this case, the predicted exhumation is $\approx$ 10% of that for the "always lithostatic" case, on average. The minimum exhumation estimate is obtained when deformation is brittle and constrictive in compression for P_p, and deformation is brittle in extension and occurs by flattening for P_r. The minimum exhumation estimate is between 0 and -50 km.

For most samples, the normalized amount of exhumation for a specific case, e.g., low stress (red rectangles), is contained within a small range around an average value. However, the samples from the category "Others (outliers)" have significantly different values. Although their values of P_p and P_r are not anomalous (e.g., Fig. 1), their combination clearly differs from other samples (see Fig. 1C). The relatively low dispersion of exhumation is related to the apparent proportionality between P_p and P_r (see Fig. 1C).

In this section, we show that one can interpret the transition from P_p to P_r as the result of exhumation from great depth (Fig. **??**C-D). The data are also compatible with an opposite interpretation: that this transition is the result of a change in stress state while depth is constant (Fig. **??**G) or even while burial continues (Fig. **??**H).

3 Two-point method of pressure-to-depth conversion

In this section, we re-examine our dataset with the additional constraint that $z_p = z_r$. In this way, we can use P_p and P_r together to reduce the uncertainty range for the depth estimate. We call this method "two-point pressure-to-depth conversion". In the case of a homogeneous rock and ignoring the possible role of fluids, the stress state can be modified in only two ways: (1) by modifying the magnitude of the horizontal stress or (2) by rotating the stress field. We explore these mechanisms independently, as well as a special case, in the following sections.

3.1 Mechanism 1: change in the magnitude of horizontal stress (S-model1)

First, we consider the change in pressure triggered by a change in the magnitude of the horizontal stress ($\bar{\sigma}_x$). Figure 6A shows five Mohr circles constructed with various values of $\bar{\sigma}_x$. Note that the Mohr circle with $\bar{\sigma}_x = 1$ is a point. In Figure 6B-J, we represent our dataset as colored circles in the P_p vs. P_r space. These data points are placed on top of a colored contour map of $\bar{\sigma}_x^r$ computed for given values of $P_p, P_r, \bar{\sigma}_x^p, \alpha_p, \alpha_r$, where subscripts or overscripts p and r refer to the peak and retrograde stages, respectively. The values used are indicated at the top of columns and the beginning of rows of panels. A contour map of $z = z_p = z_r$ is also shown (black horizontal lines). The range of values calculated for $\bar{\sigma}_x^r$ covers stress states that do not exceed the Coulomb failure criterion. Gray areas correspond to areas where $\bar{\sigma}_x^r$ has no meaningful solution (i.e., because the stress magnitude would exceed the brittle yield stress). This means that the model cannot explain data plotting in the gray area. In contrast, when a data point is on top of the colored contour map, the combination of P_p, P_r for this data point can be obtained using eqs. 13 to 16, the combination of $\bar{\sigma}_x^p, \alpha_p, \alpha_r$ given and the value of $\bar{\sigma}_x^r$ and z shown by the contour map.

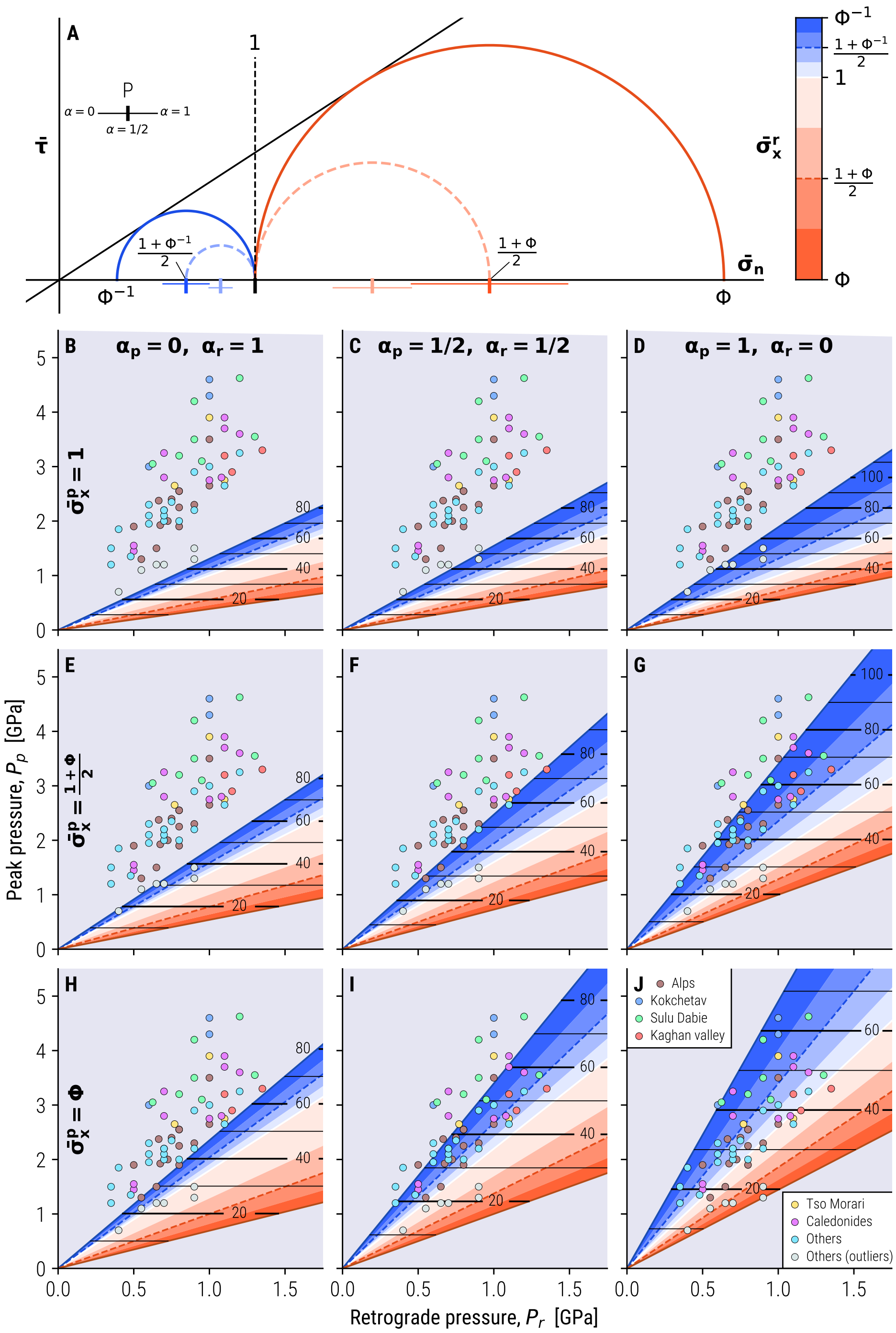

Figure 6. Results for the horizontal stress change-driven model. (J) A Mohr diagram illustrating the stress states associated with different values of $\bar{\sigma}_x$. The normal stress (horizontal axis) and shear stress (vertical axis) are normalized by σ_z. (B to J) Peak pressure as a function of retrograde pressure for data (colored circles) and model (colored contour plot). The estimated depths, in km, for each model are indicated by black contour lines. Gray areas indicate zones where the model does not have a solution (i.e., the deviatoric stress would exceed the yield stress). The model peak pressure is calculated from eq. (16) with parameters $\rho g = 28000 kg/m^2/s$, $\tan(\phi) = 0.65$, $\bar{\sigma}_x = \bar{\sigma}_x^p$, $\alpha = \alpha^p$. The model retrograde pressure uses $\bar{\sigma}_x^r$, α^r. Each panel in a row uses the value of $\bar{\sigma}_x^p$ indicated in the leftmost panel of the row. Each panel in a column uses the values of α^p and α^r indicated at the top of the column. This figure can be reproduced using the computer script from supplementary information S6.

When the stress state is lithostatic at peak conditions, i.e., $\bar{\sigma}_x^p = 1$, only outliers plot in the solution domain (Fig. 6B to D), which means that the transition from P_p to P_r observed in the data cannot be explained only by increasing or decreasing the horizontal stress at constant depth if the stress state is lithostatic under peak conditions. When the initial horizontal stress is $\bar{\sigma}_x^p = (1+\Phi)/2$, a few data points lie in the solution domain for the combinations $\alpha_p = 0, \alpha_r = 1$ (Fig. 6E) and $\alpha_p = \alpha_r = 1/2$ (Fig. 6F). However, approximately half of the points lie in the solution domain when $\alpha_p = 1, \alpha_r = 0$ (Fig. 6G). Outliers can be explained by $\bar{\sigma}_x^r > 1$ (i.e., compressive stress state), while other points are explained by $\bar{\sigma}_x^r < 1$ (i.e., extensional stress state, Fig. 6G). When the initial horizontal stress is $\bar{\sigma}_x^p = \Phi$ (i.e., brittle deformation), few data points lie in the solution domain for the combinations $\alpha_p = 0, \alpha_r = 1$ (Fig. 6H). When $\alpha_p = \alpha_r = 1/2$, half the points lie in the solution and these points correspond to values of $\bar{\sigma}_x^r < 1$ (except for outliers, Fig. 6I). When $\alpha_p = 1, \alpha_r = 0$, all the points have a solution (Fig. 6J). Most points have $\bar{\sigma}_x^r < 1$, but a few points are also associated with small values $\bar{\sigma}_x^r > 1$. Outliers are characterized by high values of $\bar{\sigma}_x^r$.

In all models except the one in Fig. 6J, some data points have a higher P_p than acceptable within the model bounds. On the other hand, there is no data point with P_p lower (or P_r higher) than that predicted by the model. The outlier points also plot within the bounds of the model. Overall, each data point is within the model boundaries or close to its boundary on at least one graph (e.g., Fig. 6J). Therefore, the model where the transition from P_p to P_r is triggered by a change in the stress state at constant depth ($z_p = z_r$) explains the data. While some points lie within the model boundaries only for a deviatoric stress with a large magnitude, other points can be explained by a change in stress with only moderate deviatoric stresses (Fig. 6G). Values of α_p, α_r are also important to explain the data; e.g., some data points can be explained only when $\alpha_p = 1, \alpha_r = 0$. For these data points, the model predicts a change in the mode of deformation from constriction to flattening during the transition from P_p to P_r. Therefore, analyses of the mode of deformation in metamorphic rock samples provide a way to validate or falsify our model.

We compute the depth depending on the given value of $\bar{\sigma}_x^p$ and α_p from eqs. 14 and 16. For $\bar{\sigma}_x \geq 1$, the pressure-to-depth conversion ratio increases with decreases in both $\bar{\sigma}_x$ and α (see Fig. 3). Graphically, this is expressed as the spacing between depth contours widening towards the right (e.g., from 6B to D) and bottom panels (e.g., from 6B to H). The cases where $\bar{\sigma}_x^p = 1$ provide the highest pressure-to-depth conversion, but only outliers lie within the solution domain. Their maximum depth is approximately 55 km (Fig. 6D). The deepest depth estimates, approximately 75 km, are obtained when $\bar{\sigma}_x^p = (1+\Phi)/2$ (Fig. 6F-G). In the case where $\bar{\sigma}_x^p = \Phi$, many points lie in the solution range, but a low pressure-to-depth conversion ratio limits the depth. Thus, the maximum depth is approximately 65 km (Fig. 6I-J). We discuss depth estimates in detail in section 3.4.

3.2 Mechanism 2: stress rotation (S-model2)

We now consider the change in pressure triggered by a rotation of the stress field. We assume that when the rock records P_p, the vertical and horizontal directions are principal stress directions, as in the previous sections. Then, the stress field rotates by an angle θ around axis y, and the rock records P_r. Figure 7A shows Mohr circles with five different values of θ.

Graphically, when we apply a rotation to a stress state where σ_1 is initially horizontal (i.e., compressional tectonic regime), the Mohr circle is shifted to the left (Fig. 7A). The maximum shift corresponds to $\theta = 90°$, and σ_1 is vertical (i.e., extensional tectonic regime). Eventually, the Mohr circle may become tangent to the Coulomb yield envelope. Since the model does not admit stress states beyond this envelope, the radius

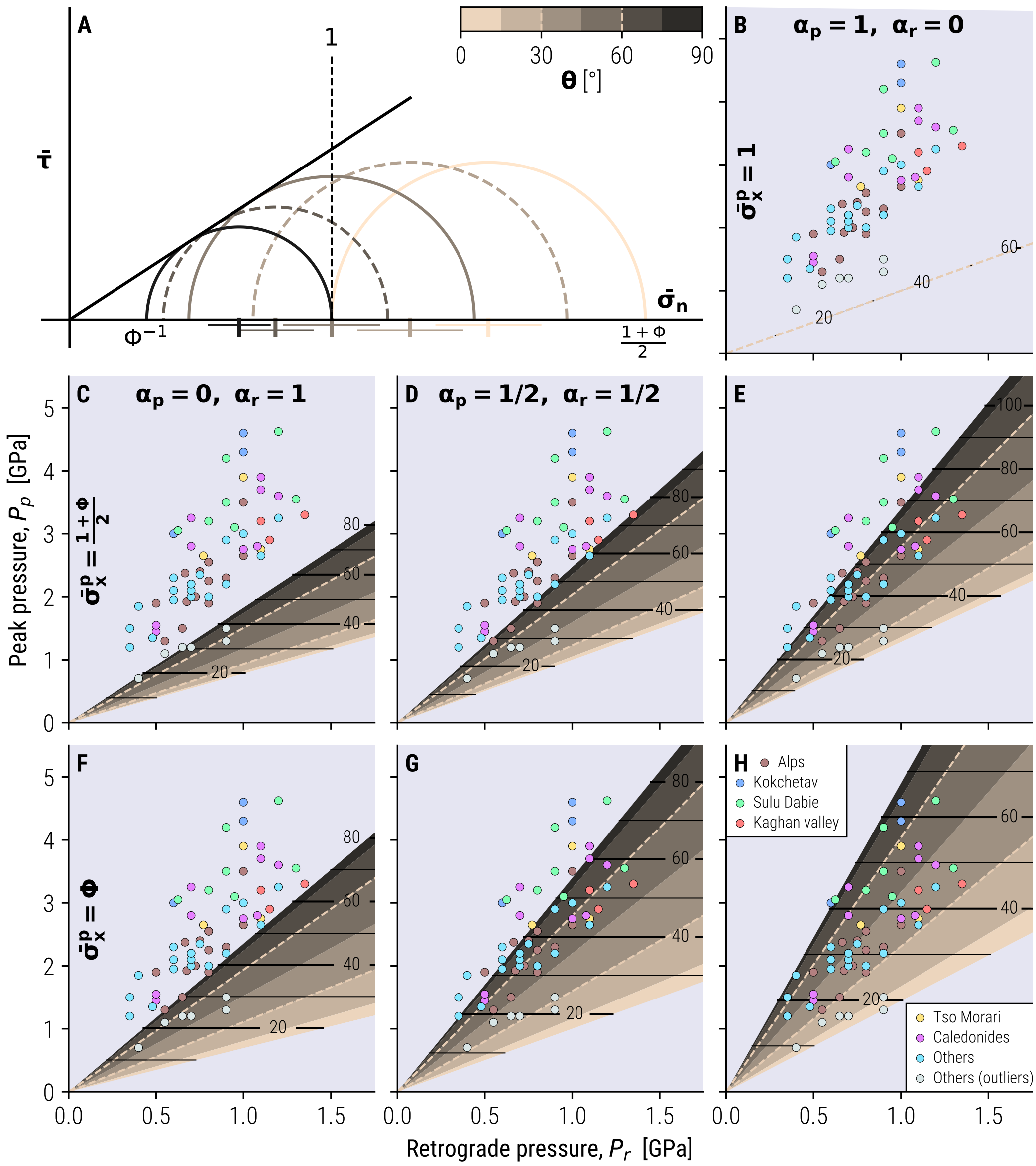

Figure 7. Summary of results for the stress rotation-driven model. θ is the counterclockwise rotation angle. (A) Mohr diagram illustrating the stress states associated with different amounts of rotation. The normal stress (horizontal axis) and shear stress (vertical axis) are normalized by σ_z. (B to H) Peak pressure as a function of retrograde pressure for different parameters (see text for details). Colored dots correspond to the data from our dataset. The estimated depths, in km, for each model are indicated by black horizontal lines. Gray areas indicate zones where the model does not have a solution. We use parameters $\rho g = 28000 kg/m^2/s$ and $\tan(\phi) = 0.65$. Each panel in a row uses the value of $\bar{\sigma}^p_x$ indicated in the leftmost panel of the row. Each panel in a column uses the values or α^p and α^r indicated at the top of the column. The colors of the contour maps are coded for values of θ. This figure can be reproduced using the computer script from supplementary information S7.

of the Mohr circle has to decrease upon further rotation to remain tangent to it (see Fig. 7A, $\theta \geq 45°$).

To formalize this behavior mathematically, we first define the yield function for Mohr-Coulomb plasticity:

$$F = \frac{\sigma_1 - \sigma_3}{2} - \frac{\sigma_1 + \sigma_3}{2} \sin \phi. \tag{18}$$

Then, the principal stresses σ_1 and σ_3 as a function of θ are expressed as

$$\text{when } F < 0, \begin{cases} \sigma_3 = \sigma_z \left(1 + (\bar{\sigma}_x^p - 1) \dfrac{\cos 2\theta - 1}{2} \right), \\ \sigma_1 = \sigma_z + \tau_{II}(\cos 2\theta + 1), \end{cases} \tag{19}$$

$$\text{when } F = 0, \begin{cases} \sigma_3 = \dfrac{2\sigma_z}{1 + \Phi - \frac{\Phi - 1}{cos2\theta}}, \\ \sigma_1 = \Phi \sigma_3. \end{cases} \tag{20}$$

Note that the first equation is only valid for $\bar{\sigma}_x^p \geq 1$. σ_2 is calculated using eq. 4, P_p is the mean stress for $\theta = 0$, and P_r is the mean stress for a given value of θ.

Figures 7B-H are constructed in the same way as Figure 6, but the brownish colored contour map now represents θ.

A lithostatic stress state is isotropic. Thus, pressure remains constant upon rotation $\bar{\sigma}_x^p = \bar{\sigma}_x^r = P_p = P_r = 1$ (Fig. 7B). The resulting line in the P_p, P_r space does not cross the data cloud, i.e., does not explain the data. For stress states tangent to the Coulomb envelope, the upper limit of the contour map for θ ($\theta = 90°$) is the same as the upper limit of $\bar{\sigma}_x^r$ ($\bar{\sigma}_x^r = 1/\Phi$) (see Fig. 6), while the lower limit ($\theta = 0°$) corresponds to the case $\bar{\sigma}_x^r = \bar{\sigma}_x^p$ in the previous model. Therefore, the boundaries of the model are similar for this model (involving θ) and for the previous model (involving $\bar{\sigma}_x^r$). Although extreme stress states are identical, intermediate cases are different (e.g., compare Figs. 6A and 7A). When $\bar{\sigma}_x^p = (1 + \Phi)/2$, a minimum of $\theta = 45°$ is required to explain the data (Fig. 7C-E). As with the previous model, all data points are consistent with a model where $\bar{\sigma}_x^p = \Phi, \alpha_p = 1, \alpha_r = 0$ (Fig. 7H). In this case, outliers are explained by $\theta = 0-30°$ and other points by $\theta = 30-90°$. Since the depth contour map is computed based on $\bar{\sigma}_x^p, \alpha_p$ only and the model range is similar to the previous model, the remarks concerning depth made in section 3.1 also apply here.

Since both this model (Fig. 6) and the previous one (Fig. 7) can explain the data, there is an ambiguity about which mechanism is responsible for the stress change. Once again, the predictions of this model can be validated or falsified using strain data. Indeed, the rotation of the principal stress directions implies a rotation of the principal strain direction.

3.3 A special case: compression to extension in the brittle limit (YB-model)

When $\bar{\sigma}_x^p = \Phi$, depending on the values of α_p, α_r, the solution for $\theta = 90°$ (which corresponds to the upper limit of the solution domain) can outline the lower extent of the data point cloud (Fig. 7F), pass through it (Fig. 7G), or outline its upper extent (Fig. 7H). In other terms, the data distribution can also be explained by a more restrictive model where depth is constant, $\bar{\sigma}_x^p = \Phi$, $\theta = 90°$ (or $\bar{\sigma}_x^r = 1/\Phi$, cf. Fig. 6) and α_p and α_r are free parameters. This model has previously been employed by Yamato and Brun (2017). Here, we extend their analysis by providing the associated pressure-to-depth conversion.

To obtain a mathematical expression for P_p, we substitute eq. (14) with $\bar{\sigma}_x = \Phi$ for $\bar{P}$ in eq. (16) and solve for P. For P_r, we use eq. (13) with $\bar{\sigma}_x = 1/\Phi$ instead of eq.

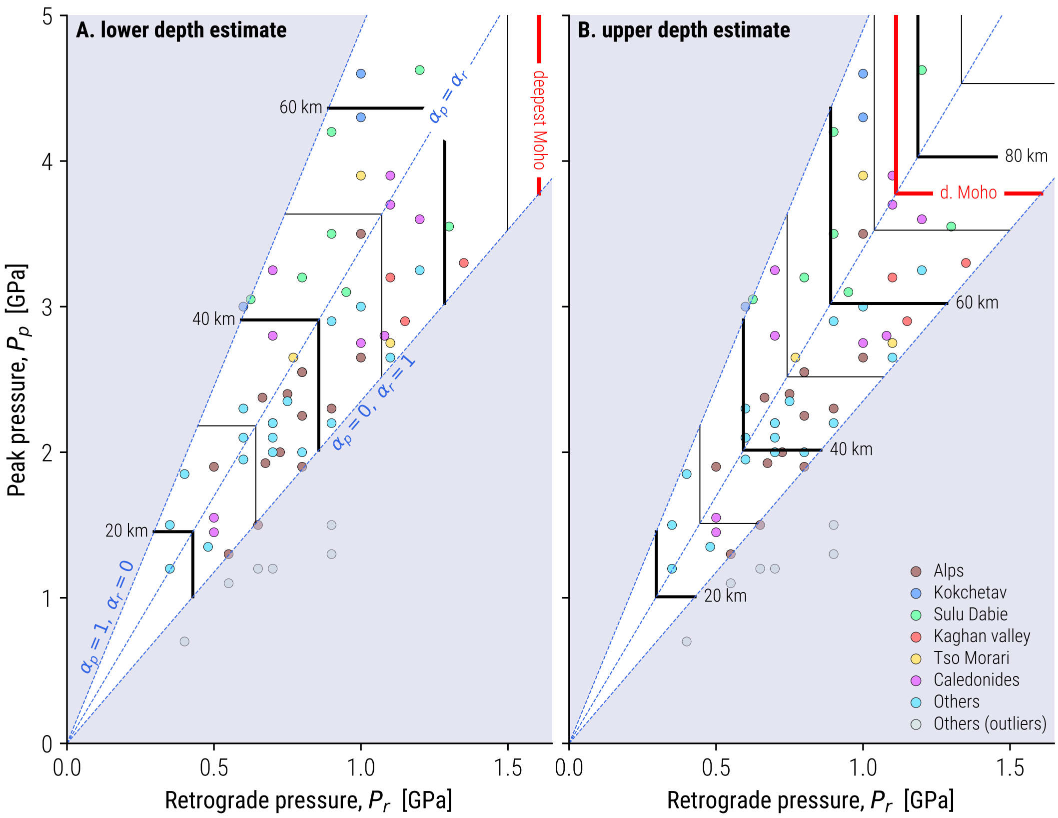

Figure 8. Data points in the P_p vs. P_r space. Contours of depth according to (a) the lower estimate and (b) upper estimate of our model. The model has solutions within the white fan and no solution in the gray domain. The color of the data points indicates the geographic region. This figure can be reproduced using the computer script from supplementary information S8.

(14). This process yields:

$$P_p = \frac{\rho g z}{3}(2 - \alpha^p + \Phi(1 + \alpha^p)), \tag{21}$$

$$P_r = \frac{\rho g z}{3}(1 + \alpha^r + \Phi^{-1}(2 - \alpha^r)). \tag{22}$$

Similar to previous figures, Figure 8 shows the domain of the solution of eqs. (21) and (22) for values of α_p and α_r between 0 and 1. Data points are also plotted in this P_p vs. P_r space. We also show contours of depth obtained by solving eq. (21) or (22) for z. The value of ρg influences the distance between depth contours but not the shape of the solution domain. The parameter Φ (or ϕ, cf eq. 11) controls the orientation and opening angle of the fan-shaped solution domain. The outlier points (gray) lie outside the solution domain, while the other data points (colored) lie within it or close to its boundary. The location of a point within the solution domain reflects the depth and mode of deformation under peak and retrograde conditions (α_p, α_r). Points along the central line $\alpha_p = \alpha_r$ have the same mode of deformation in the peak and retrograde stages. Points below this line deform by flattening under peak conditions and by constriction under retrograde conditions, and points lying above the central line deform by constriction under peak conditions and by flattening under retrograde conditions. Samples from one orogen tend to span a large range of α_p, α_r that could reflect local differences in the mode of deformation.

For a given depth, a range of P_p, P_r is possible depending on the value of α_r, α_p (see eqs. 21 and 22). The opposite is also true: for a given P_p, P_r, there is a range of possible depths. We represent the lower and upper estimates of this range in Figures 8A and 8B, respectively. In this model, all points lie below the "deepest Moho" reference depth for the lower depth estimate, and only one point is deeper than the "deepest Moho" when using the upper depth estimate.

3.4 Depth estimates using the two-point method

Figure 9 shows depth estimates for our data according to the horizontal stress change-driven model and the stress rotation model ("S-model", thin bars) and the compression to extension model of the previous section ("YB-model", thick bars). Depth estimates for peak pressure assuming a lithostatic stress state (see section 2.3) are also shown as the "L model" for reference (short bars).

In the following passage, we use the terms L-depth, S-depth and YB-depth to refer to the depth estimates according to the L-, S- and YB-models, respectively. The methods for computing the depth ranges for the S-model and YB-model are given in Appendix A.

The minimum and maximum YB-depths are equal for points on the border of the solution domain fan, while the range is largest for points along the central line (Fig. 8). The range of S-depth tends to be larger for points with a low P_p/P_r ratio and decreases with increasing P_p/P_r (because fewer solutions exist; see Figs. 6 and 7). For all samples except the outliers, the S- and YB-depths are significantly lower than the L-depth. For example, one point in Kokchetav and one point in Sulu-Dabie have L-depths > 160 km, whereas their S- and YB-depths are $65-70$ km and $60-85$ km, respectively. For outliers, the upper estimate of the S-depth is close to the L-depth. In the L-model, the depth is proportional to the peak pressure. Thus, large differences in peak pressure between two samples result in large differences in depth. However, the S- and YB-models take both peak and retrograde pressures into account, which can smooth out this difference. For example, the two data points with the highest pressures in the Alps have L-depths of 95 and 125 km, whereas the maximum S-depth is 70 km for both. Conversely, points with the same L-depth (i.e., same peak pressure) can have different YB- and S-depths. This contrast is best exemplified by comparing points with the same P_p in Figure 8: points

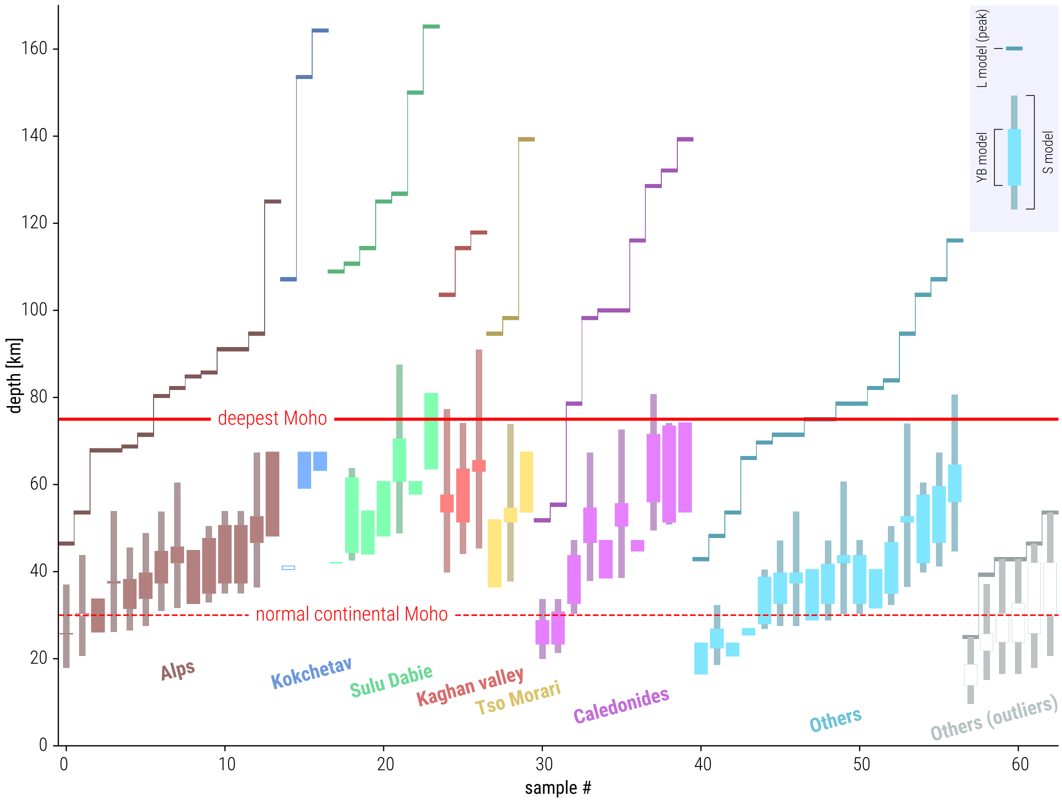

Figure 9. Estimated depth of each sample using the two-point method of pressure-to-depth conversion. The graph also shows depth estimates using the one-point lithostatic case for reference. L-model: peak pressure in the one-point lithostatic case. S-model refers to the models described in sections 3.1 and 3.2. The YB-model refers to the model described in section 3.3. For the YB-model, filled rectangles indicate depth estimates for points that lie within the model boundaries, while open rectangles apply to points outside the model boundaries. The depth estimates indicated by open rectangles are relevant for points close to the model boundary (e.g., samples #1 and #14) but less relevant for points far from the boundary (i.e., category Others (outliers)). This figure can be reproduced using the computer script from supplementary information S9.

in the upper half of the fan ($\alpha_p > \alpha_r$) align on a lower depth estimate contour, while points in the lower half of the fan ($\alpha_p < \alpha_r$) align on the upper depth estimate contour. Thus, at constant P_p, the mean depth estimate increases with increasing P_r, and the uncertainty increases towards the center of the fan ($\alpha_p = \alpha_r$ line). For example, for points at $P_p = 3GPa$, the mean depth estimate increases from 40 km at $P_r = 0.6GPa$ to 60 km at $P_r = 1.2GPa$. At these two extreme P_r values, the depth estimate has a unique value, while at the center of the fan ($P_r = 0.85GPa$), the depth estimate ranges between 40 and 60 km. Overall, the most striking features of the S- and YB-models are that all data points have at least part of their range shallower than the "deepest Moho" line and that the deepest S-depth is approximately 90 km compared to 165 km for the L-depth.

4 Discussion

Pressure is a function of both depth and deviatoric stresses. However, since deviatoric stress cannot be measured, pressure-to-depth conversions require assumptions. In the previous sections, we propose several pressure-to-depth conversion methods involving one or two pressure data points. In particular, we show that the proportionality between P_p and P_r can be explained by a model where P_p and P_r are recorded by the rock at the same depth but under different stress states (Figs. 6 to 8). For simplicity, we only present two-point models with either stress rotation or horizontal stress magnitude change and no exhumation. Combining rotation and magnitude change may further decrease the magnitude of deviatoric stresses required to explain the data. Relaxing the assumption that $z_p = z_r$ and accounting for some exhumation would also decrease the magnitude of deviatoric stresses required.

4.1 Perspectives on using strain data

In our formulation of the pressure-to-depth conversion, we use α instead of a stress value (see eq. 4). α characterizes the shape of the stress ellipsoid and is thus similar to commonly used parameters for characterizing the shape of ellipsoid such as Lode's ratio or Flinn's k-value (Mookerjee & Peek, 2014). Because strain results from applied stress, obtaining a value for α using markers of deformation could provide key data to better constrain depth. The two-point models relying on a change in the magnitude of horizontal stress (Fig. 6) or stress orientation (Fig. 7) give ambiguous results since both models can explain the data. However, one could falsify the predictions of the model based on stress rotation (Fig. 7) by using the directions of the strain ellipsoid or paleostress inversion of fault orientations to estimate stress directions.

4.2 Data distribution and model

The data suggest that P_p and P_r are proportional (see Fig. 1). However, by using the one-point method, because P_p and P_r are considered independently, it is difficult to explain this proportionality. In the lithostatic case, for instance, the decompression from P_p to P_r is controlled only by the exhumation of rocks. However, the currently proposed exhumation mechanisms (e.g., subduction channels and corner flows) do not suggest that exhumation would be proportional to maximum depth. On the other hand, the two-point model treats both P_p and P_r together. Since we assume that $z_p = z_r$, the maximum change from P_p to P_r is limited by Byerlee's law, and the yield stress function is linearly dependent on P. Considering reasonable values for the friction coefficient (e.g., 0.65), the limits of the model outline the distribution of the data. For example, for the models shown in Figures 6J and 7H, the extent of the model domain outlines the upper extent of the distribution, and the lower limit of the model corresponds to the lower extent for outliers.

The YB-model simulates the case where rocks are brittle in both compression and extension and thus constitutes a particular case of the two-point model. It is interesting to note that although the YB-model allows us to largely explain the data, it excludes the outliers (Fig. 8). However, all data (including outliers) can be explained considering the more general S-models (Figs. 6 and 7).

The upper extent of the data distribution (P_p/P_r 4.8) can only be explained when $\bar{\sigma}_x^p = \Phi, \alpha_p = 1$ (brittle constrictive deformation in compression) and $\bar{\sigma}_x^r = 1/\Phi, \alpha_r = 0$ (brittle flattening deformation in extension). The lower extent of the data distribution excluding outliers (P_p/P_r 2.4), however, can have several explanations. In the YB-model, it corresponds to $\alpha_p = 0, \alpha_r = 1$. For S-models (e.g., Figs. 6G, I, J; 7E, G, H), the lower bound of the data can be within the solution domain and coincides with different values of $\bar{\sigma}_x^r$ or θ. Interestingly, the lower limit coincides with Sxr=1 (i.e., lithostatic case) in Fig. 6J. Two-point models can fit all data points from the dataset (or lie very close to the model boundary), which suggests that in all orogens, a change in stress state may be responsible for the decompression from P_p to P_r. The different predictions in terms of the change mode of deformation (α_p to α_r) bring additional constraints concerning the mechanism responsible for the change in the stress state. Monitoring the evolution of α in 3D numerical geodynamic models may provide more answers.

4.3 Inclusion-host system

The models presented here explain pressure variations in a homogeneous material subjected to a change in depth or deviatoric stresses. In a heterogeneous system, the pressure in one material may be affected by deviatoric stresses in another material. A well-studied example is the case of an elliptical inclusion embedded in an elastic or linear viscous matrix. In this system, the magnitude and sense of deviatoric stresses are functions of the relative strength between the matrix and the inclusion, as well as the orientation of the inclusion in the stress field (D. W. Schmid & Podladchikov, 2003, 2005; Moulas et al., 2014). The pressure in the inclusion is controlled both by the stress state in the inclusion and by the stress state in the host rock. An important point is that deviatoric stresses in a weak inclusion may be negligible, while the pressure can still be as high as $\sigma_1 = \Phi$ in a strong host rock. This is very different from a homogeneous material where the pressure is lithostatic in the absence of deviatoric stresses. Thus, pressure can vary between the values of σ_3 and σ_1 for the strongest material in the inclusion/host system, whereas in a homogeneous material, pressure can vary only between $2/3\sigma_3+1/3\sigma_1$ and $1/3\sigma_3+2/3\sigma_1$ (see eq. (6)) (Moulas et al., 2014; Schmalholz & Podladchikov, 2013). Field examples of this phenomenon have been documented by Luisier et al. (2019) in the Monte Rosa nappe (Alps) and by Jamtveit et al. (2018) in the Bergen Arc (Caledonides).

4.4 Local vs. regional stress state

In this paper, we present several methods that can be used to determine possible stress states associated with peak and metamorphic pressures. Stress states are by essence local. Some researchers even propose that metamorphic pressure may reflect the stress state in only a single grain (see the discussion about inclusions in the previous paragraph) and that large pressure gradients responsible for pressure differences on the order of GPa can be recorded within a single grain (Tajčmanová et al., 2014, 2015). In our dataset, samples from the same region have a wide variety of P_p/P_r ratios (see Fig. 1C) and are often distributed from one side of the fan to another (between $P_p/P_r = 1.4$ and $P_p/P_r = 4.8$), which indicates differences in the change in stress magnitude, stress orientation or relative magnitude of σ_2 (α). This could be an indication that pressure data reflect the local (grain- to 10 km-scale) rather than regional (100 km) stress state. Thus, using the stress states determined in this study to interpret regional-scale processes requires taking some caution. For example, the YB-model assumes that the peak to retrograde pressure can be explained by a transition from a compressional to an extensional stress state, with both stress states close to the brittle limit. These stress states reflect km-scale conditions or are smaller in the sense that the whole system is submitted to convergence (i.e., in Fig. 1). The distance between two points far from the subduction zone, one located on the subducting plate and the other located on the overriding plate, is constantly decreasing, but the part undergoing exhumation is locally subjected to extension. This corresponds well with the fact that the exhumation of a coherent metamorphic unit is impossible without a normal fault on top. As we have shown, stress orientation has a strong control on pressure changes, and in a complex orogen, stress orientations can vary significantly in space and time, e.g., due to changes in the subduction angle or the friction along the plate boundary (Wang & Hu, 2006), the proximity to magma chambers (Gerbault et al., 2018) or faults (e.g., Shao & Hou, 2019; Martínez-Díaz, 2002; Maerten et al., 2002), or the position within the orogen (e.g., Kastrup et al., 2004).

4.5 Implications for geodynamic models

Rock strength strongly depends on temperature. Hence, considering classic rheological yield stress envelopes (e.g., E. B. Burov, 2011), it seems inadequate to consider large deviatoric stresses deep in the lithosphere ($>$ 120 km) due to the temperature increase with depth. This statement could favor using lithostatic pressure-to-depth conversion but remains debatable. Indeed, the depth estimates using the S- and YB-models are consistent with the depth of the crustal roots of orogens, and in these places (i.e., at the base of the crust or in the lithospheric mantle), significant deviatoric stresses are possible. Significant deviatoric stresses are even more likely at this depth in a subduction zone with a cold geotherm.

Several elements suggest significant deviatoric stresses near the Moho depth: (1) earthquakes are not uncommon at such depths in a subduction context and provide evidence that brittle deformation can occur (e.g., B. Hacker et al., 2003; Hetényi et al., 2007), and (2) several field and petrological studies have already evidenced brittle deformation associated with HP metamorphism (e.g., Austrheim & Boundy, 1994; John & Schenk, 2006; Angiboust et al., 2012; Hertgen et al., 2017; Yang et al., 2014).

Samples with high P_p/P_r require a stress field close to the brittle limit using the S-model (e.g., Fig. 7). However, samples with $P_p/P_r < \Phi$ are consistent with a stress state where the magnitude of the deviatoric stress (second invariant) is only half that required for brittle deformation (i.e., $\bar{\sigma}_x^p = (1+\Phi)/2$) when peak pressure is recorded. This means that even in the ductile realm, the effect of the deviatoric stresses should not be neglected.

The release of fluids from dewatering metamorphic reactions can decrease the effective pressure. Thus, one might argue that the transition from P_p to P_r is caused by fluid pressure. However, this mechanism seems unlikely because fluid pressure would need to remain high during exhumation (otherwise, a new peak pressure would be recorded). Townend and Zoback (2000) argue that high fluid pressure leads to rock fracturing, which creates space and thus causes fluid pressure to decrease.

5 Conclusion

In this contribution, we reviewed the basic mathematical formulations of pressure-to-depth conversion for a homogeneous rock. First, we derived the standard "one-point method of pressure-to-depth conversion" and applied it to a large dataset of metamorphic pressures to independently estimate a range of depths at which rocks may have recoded their peak (P_p) and retrograde pressures (P_r). Since the most common assumption in the literature is to consider that metamorphic pressure corresponds to the lithostatic pressure, we used this "lithostatic case" as a reference.

By introducing deviatoric stress components and considering only the compressional stress regime (σ_1 horizontal) at P_p and both compressional and extensional (σ_1 vertical) stress regimes for P_r, we showed that the deviations from the reference case can be significant. For P_p, the estimated depths vary between 40 and 100 % of the reference case. For P_r, the estimated depth range is $40-185\%$ of the reference case. Thus, under our assumption, the lithostatic case represents an upper bound estimate of depth for P_p and an intermediate value for P_r. Moreover, the uncertainty ranges of both peak (z_p) and retrograde (z_r) depths are large enough to lead to overlap for these two depth estimates. This means that the transition from P_p to P_r can be triggered by exhumation, a change in the stress state at constant depth, or a combination of both processes.

Second, we presented "two-point methods of pressure-to-depth conversion" that use both P_p and P_r to estimate depth under the hypothesis that $z_p = z_r$. For the two-point method, we considered two mechanisms of stress change between P_p and P_r: (1)

change in the magnitude of horizontal stresses and (2) rotation of the stress state. We also treated a particular case where the magnitude of deviatoric stresses is maximum, and the stress regime varies from compression at P_p to extension at P_r. The two-point method greatly decreases the uncertainty range of depth estimates and yields stricter constraints on the possible stress state. Remarkably, all P_p, P_r points in our dataset are consistent with a change in the stress state at a constant depth.

In our dataset, the maximum depth estimates under the "lithostatic assumption" are approximately 160 km for P_p and 50 km for P_r. Thus, the lithostatic assumption requires deep burial and exhumation from great depth. On the other hand, the two-point models reveal that points in our dataset are consistent with depths shallower than 75 km (i.e., the current deepest Moho). This suggests instead that all metamorphic rocks in our dataset have been buried at crustal depths with no (or only minor) exhumation between P_p and P_r. The validity of either of these models cannot be assessed based only on pressure and temperature data. However, the principal stress directions and the relative magnitude of σ_2 (i.e., α) may be estimated from the strain ellipsoid or paleostress analysis. Thus, a precise analysis of the deformation in association with the P estimates in metamorphic rocks could validate or falsify depth estimates from the two-point model and further decrease the depth estimate uncertainty.

Appendix A Depth estimates for the two-point model

A1 S-model

The depth estimate range for S-models is calculated numerically by testing a large array of combinations of $\bar{\sigma}_x^p$, α_p and α_r for each sample. The ranges considered are $1 \leq \bar{\sigma}_x^p \leq \Phi$ and $0 \leq \alpha_p, \alpha_r \leq 1$, and we use 50 values to discretize the range of each parameter for a total of $50^3 = 125,000$ parameter combinations. We proceed in two steps. First, we compute σ_z using eq. (15) with $P = P_p$, $\bar{\sigma}_x = \bar{\sigma}_x^p$, and $\alpha = \alpha_p$, and we compute $z = \sigma_z/\rho g$. Second, we need to test whether the previous solution is within the acceptable bounds of the model (i.e., not in the gray area of Figs. 6 to 8). For this purpose, we compute $\bar{\sigma}_x^r$ using the following equation:

$$\begin{cases} \bar{\sigma}_x = \dfrac{3P/\sigma_z - 2 + \alpha}{1 + \alpha}, \text{ when } \bar{\sigma}_x \leq 0, \\ \bar{\sigma}_x = \dfrac{3P/\sigma_z - 1 - \alpha}{2 - \alpha}, \text{ when } \bar{\sigma}_x \geq 0, \end{cases} \tag{A1}$$

with $P = P_r$, $\bar{\sigma}_x = \bar{\sigma}_x^r$, and $\alpha = \alpha_r$. Then, we test whether $1/\Phi \leq \bar{\sigma}_x^r \leq \Phi$ and update the range of depth if the test is successful.

A2 YB-model

To compute the range of depth for the YB-model, we use the minimum and upper estimates of depth whose contours are plotted in Figures 8A and 8B, respectively. In practice, we compute σ_z using eq. (15) with parameters $[P, \alpha, \bar{\sigma}_x]$. For data points where $P_p/P_r > \Phi$ (i.e., above the line marked $\alpha_p = \alpha_r$ in Fig. 8), we use parameters $[P_p, 1, \Phi]$ to compute $min(\sigma_z)$, and $[P_r, 0, 1/\Phi]$ for $max(\sigma_z)$. For data points where $P_p/P_r \leq \Phi$, we use $[P_r, 1, 1/\Phi]$ for $min(\sigma_z)$ and $[P_p, 0, \Phi]$ for $max(\sigma_z)$. Then, we compute $z = \sigma_z/\rho g$. In this algorithm, depth is calculated using either $[P_p, \alpha_p, \bar{\sigma}_x^p]$ or $[P_r, \alpha_r, \bar{\sigma}_x^r]$. If α_p is used as input, α_r can be computed back from σ_z, and we can perform the test $0 \leq \alpha_r \leq 1$ to verify that the solution is within the bounds of the model. If α_r is used as input, α_p is computed instead. If the test is successful, we plot the range as a colored box in Figure 9 or as an open box otherwise.

Acknowledgments

The database and computer code (Jupyter notebooks) allowing the reproduction of most figures are available as supplementary information and will be made available in a public repository once the paper is accepted for publication. This work was supported by the Japanese Society for the Promotion of Science (JSPS), Grant-in-Aid for Scientific Research no. JP18K13643.

References

Agard, P., Yamato, P., Jolivet, L., & Burov, E. (2009, jan). *Exhumation of oceanic blueschists and eclogites in subduction zones: Timing and mechanisms* (Vol. 92) (No. 1-2). Elsevier. doi: 10.1016/j.earscirev.2008.11.002

Anderson, E. M. (1905, jan). The dynamics of faulting. *Transactions of the Edinburgh Geological Society*, *8*(3), 387–402. doi: 10.1144/transed.8.3.387

Angiboust, S., Agard, P., Yamato, P., & Raimbourg, H. (2012, aug). Eclogite breccias in a subducted ophiolite: A record of intermediatedepth earthquakes? *Geology*, *40*(8), 707–710. doi: 10.1130/G32925.1

Austrheim, H., & Boundy, T. M. (1994). Pseudotachylytes generated during seismic faulting and eclogitization of the deep crust. *Science*, *265*(5168), 82–83. doi: 10.1126/science.265.5168.82

Beaumont, C., Jamieson, R. A., Butler, J. P., & Warren, C. J. (2009, sep). Crustal structure: A key constraint on the mechanism of ultra-high-pressure rock exhumation. *Earth and Planetary Science Letters*, *287*(1-2), 116–129. doi: 10.1016/j.epsl.2009.08.001

Beltrando, M., Hermann, J., Lister, G., & Compagnoni, R. (2007, apr). On the evolution of orogens: Pressure cycles and deformation mode switches. *Earth and Planetary Science Letters*, *256*(3-4), 372–388. doi: 10.1016/j.epsl.2007.01.022

Brace, W. F., Ernst, W. G., & Kallberg, R. W. (1970, may). An Experimental Study of Tectonic Overpressure in Franciscan Rocks. *GSA Bulletin*, *81*(5), 1325–1338. doi: 10.1130/0016-7606(1970)81[1325:aesoto]2.0.co;2

Brun, J. P., & Faccenna, C. (2008, jul). Exhumation of high-pressure rocks driven by slab rollback. *Earth and Planetary Science Letters*, *272*(1-2), 1–7. doi: 10.1016/j.epsl.2008.02.038

Burov, E., Francois, T., Yamato, P., & Wolf, S. (2014, mar). Mechanisms of continental subduction and exhumation of HP and UHP rocks. *Gondwana Research*, *25*(2), 464–493. doi: 10.1016/j.gr.2012.09.010

Burov, E. B. (2011, aug). Rheology and strength of the lithosphere. *Marine and Petroleum Geology*, *28*(8), 1402–1443. doi: 10.1016/j.marpetgeo.2011.05.008

Butler, J. P., Beaumont, C., & Jamieson, R. A. (2013, sep). The Alps 1: A working geodynamic model for burial and exhumation of (ultra)high-pressure rocks in Alpine-type orogens. *Earth and Planetary Science Letters*, *377-378*, 114–131. doi: 10.1016/j.epsl.2013.06.039

Butler, J. P., Beaumont, C., & Jamieson, R. A. (2014, jul). The Alps 2: Controls on crustal subduction and (ultra)high-pressure rock exhumation in Alpine-type orogens. *Journal of Geophysical Research: Solid Earth*, *119*(7), 5987–6022. Retrieved from `http://doi.wiley.com/10.1002/2013JB010799` doi: 10.1002/2013JB010799

Byerlee, J. (1978, jul). Friction of rocks. *Pure and Applied Geophysics PAGEOPH*, *116*(4-5), 615–626. doi: 10.1007/BF00876528

Chopin, C. (2003, jul). Ultrahigh-pressure metamorphism: Tracing continental crust into the mantle. *Earth and Planetary Science Letters*, *212*(1-2), 1–14. doi: 10.1016/S0012-821X(03)00261-9

Ernst, W. G. (1963). Significance Of Phengitic Micas From Low-Grade Schists — American Mineralogist — GeoScienceWorld. *American Mineralogist*, *48*(11-

12), 1357–1373. Retrieved from https://pubs.geoscienceworld.org/msa/ammin/article-abstract/48/11-12/1357/542168

Ernst, W. G., Hacker, B. R., & Liou, J. G. (2007). Petrotectonics of ultrahigh-pressure crustal and upper-mantle rocks—Implications for Phanerozoic collisional orogens. *Geol. Soc. Am.*, *433*, 27–49.

Froitzheim, N., Pleuger, J., Roller, S., & Nagel, T. (2003, oct). Exhumation of high- and ultrahigh-pressure metamorphic rocks by slab extraction. *Geology*, *31*(10), 925–928. doi: 10.1130/G19748.1

Gerbault, M., Hassani, R., Novoa Lizama, C., & Souche, A. (2018, mar). Three-Dimensional Failure Patterns Around an Inflating Magmatic Chamber. *Geochemistry, Geophysics, Geosystems*, *19*(3), 749–771. Retrieved from http://doi.wiley.com/10.1002/2017GC007174 doi: 10.1002/2017GC007174

Gerya, T. (2015, oct). Tectonic overpressure and underpressure in lithospheric tectonics and metamorphism. *Journal of Metamorphic Geology*, *33*(8), 785–800. Retrieved from http://doi.wiley.com/10.1111/jmg.12144 doi: 10.1111/jmg.12144

Godard, G. (2001, aug). Eclogites and their geodynamics interpretation: A history. *Journal of Geodynamics*, *32*(1-2), 165–203. doi: 10.1016/S0264-3707(01)00020-5

Green, H. W. (2005). Psychology of a changing paradigm: 40+ Years of high-pressure metamorphism. *International Geology Review*, *47*(5), 439–456. doi: 10.2747/0020-6814.47.5.439

Guillot, S., Hattori, K., Agard, P., Schwartz, S., & Vidal, O. (2009). Exhumation Processes in Oceanic and Continental Subduction Contexts: A Review. In *Subduction zone geodynamics* (pp. 175–205). Springer Berlin Heidelberg. doi: 10.1007/978-3-540-87974-9_10

Hacker, B., Peacock, S., Abers, G., & Holloway, S. (2003). Subduction factory 2. Are intermediate-depth earthquakes in subducting slabs linked to metamorphic dehydration reactions? *J. Geophys. Res.*, *108*, 2030.

Hacker, B. R., & Gerya, T. V. (2013, sep). *Paradigms, new and old, for ultrahigh-pressure tectonism* (Vol. 603). doi: 10.1016/j.tecto.2013.05.026

Hertgen, S., Yamato, P., Morales, L. F., & Angiboust, S. (2017, jun). Evidence for brittle deformation events at eclogite-facies P-T conditions (example of the Mt. Emilius klippe, Western Alps). *Tectonophysics*, *706-707*, 1–13. doi: 10.1016/j.tecto.2017.03.028

Hetényi, G., Cattin, R., Brunet, F., Bollinger, L., Vergne, J., Nábělek, J. L., & Diament, M. (2007, dec). Density distribution of the India plate beneath the Tibetan plateau: Geophysical and petrological constraints on the kinetics of lower-crustal eclogitization. *Earth and Planetary Science Letters*, *264*(1-2), 226–244. doi: 10.1016/j.epsl.2007.09.036

Hobbs, B., & Ord, A. (2015, nov). *Dramatic effects of stress on metamorphic reactions: COMMENT* (Vol. 43) (No. 11). Geological Society of America. doi: 10.1130/G37070C.1

Hobbs, B. E., & Ord, A. (2017, dec). Pressure and equilibrium in deforming rocks. *Journal of Metamorphic Geology*, *35*(9), 967–982. Retrieved from http://doi.wiley.com/10.1111/jmg.12263 doi: 10.1111/jmg.12263

Huw Davies, J., & von Blanckenburg, F. (1995, jan). Slab breakoff: A model of lithosphere detachment and its test in the magmatism and deformation of collisional orogens. *Earth and Planetary Science Letters*, *129*(1-4), 85–102. doi: 10.1016/0012-821X(94)00237-S

Jamieson, J. C. (1963, aug). Possible occurence of exceedingly high pressures in geological processes. *GSA Bulletin*, *74*(8), 1067–1070. doi: 10.1130/0016-7606(1963)74[1067:pooehp]2.0.co;2

Jamtveit, B., Moulas, E., Andersen, T. B., Austrheim, H., Corfu, F., Petley-Ragan, A., & Schmalholz, S. M. (2018, dec). High Pressure Metamorphism Caused by

Fluid Induced Weakening of Deep Continental Crust. *Scientific Reports*, *8*(1), 1–8. doi: 10.1038/s41598-018-35200-1

John, T., & Schenk, V. (2006, jul). Interrelations between intermediate-depth earthquakes and fluid flow within subducting oceanic plates: Constraints from eclogite facies pseudotachylytes. *Geology*, *34*(7), 557–560. doi: 10.1130/G22411.1

Kastrup, U., Zoback, M. L., Deichmann, N., Evans, K. F., Giardini, D., & Michael, A. J. (2004, jan). Stress field variations in the Swiss Alps and the northern Alpine foreland derived from inversion of fault plane solutions. *Journal of Geophysical Research: Solid Earth*, *109*(B1). doi: 10.1029/2003jb002550

Luisier, C., Baumgartner, L., Schmalholz, S. M., Siron, G., & Vennemann, T. (2019, dec). Metamorphic pressure variation in a coherent Alpine nappe challenges lithostatic pressure paradigm. *Nature Communications*, *10*(1), 1–11. doi: 10.1038/s41467-019-12727-z

Maerten, L., Gillespie, P., & Pollard, D. D. (2002, jan). Effects of local stress perturbation on secondary fault development. *Journal of Structural Geology*, *24*(1), 145–153. doi: 10.1016/S0191-8141(01)00054-2

Mancktelow, N. S. (1993, nov). Tectonic overpressure in competent mafic layers and the development of isolated eclogites. *Journal of Metamorphic Geology*, *11*(6), 801–812. Retrieved from `http://doi.wiley.com/10.1111/j.1525-1314.1993.tb00190.x` doi: 10.1111/j.1525-1314.1993.tb00190.x

Mancktelow, N. S. (2008, jun). Tectonic pressure: Theoretical concepts and modelled examples. *Lithos*, *103*(1-2), 149–177. Retrieved from `https://www.sciencedirect.com/science/article/pii/S002449370700223X{\#}bib83` doi: 10.1016/J.LITHOS.2007.09.013

Martínez-Díaz, J. J. (2002, oct). Stress field variation related to fault interaction in a reverse oblique-slip fault: The Alhama de Murcia fault, Betic Cordillera, Spain. *Tectonophysics*, *356*(4), 291–305. doi: 10.1016/S0040-1951(02)00400-6

Mookerjee, M., & Peek, S. (2014, nov). Evaluating the effectiveness of Flinn's k-value versus Lode's ratio. *Journal of Structural Geology*, *68*(PA), 33–43. doi: 10.1016/j.jsg.2014.08.008

Moulas, E., Burg, J. P., & Podladchikov, Y. (2014). Stress field associated with elliptical inclusions in a deforming matrix: Mathematical model and implications for tectonic overpressure in the lithosphere. *Tectonophysics*, *631*(C), 37–49. doi: 10.1016/j.tecto.2014.05.004

Moulas, E., Podladchikov, Y. Y., Aranovich, L. Y., & Kostopoulos, D. (2013, nov). The problem of depth in geology: When pressure does not translate into depth. *Petrology*, *21*(6), 527–538. doi: 10.1134/S0869591113060052

Moulas, E., Schmalholz, S. M., Podladchikov, Y., Tajčmanová, L., Kostopoulos, D., & Baumgartner, L. (2019). Relation between mean stress, thermodynamic, and lithostatic pressure. *Journal of Metamorphic Geology*, *37*(1), 1–14. doi: 10.1111/jmg.12446

Nagel, T. J. (2008, jan). Tertiary subduction, collision and exhumation recorded in the Adula nappe, central Alps. *Geological Society Special Publication*, *298*(1), 365–392. doi: 10.1144/SP298.17

Parrish, R. R., Gough, S. J., Searle, M. P., & Waters, D. J. (2006, nov). Plate velocity exhumation of ultrahigh-pressure eclogites in the Pakistan Himalaya. *Geology*, *34*(11), 989–992. doi: 10.1130/G22796A.1

Petrini, & Podladchikov. (2000, jan). Lithospheric pressure-depth relationship in compressive regions of thickened crust. *Journal of Metamorphic Geology*, *18*(1), 67–77. Retrieved from `http://doi.wiley.com/10.1046/j.1525-1314.2000.00240.x` doi: 10.1046/j.1525-1314.2000.00240.x

Platt, J. P. (1986, sep). Dynamics of orogenic wedges and the uplift of high-pressure metamorphic rocks. *GSA Bulletin*, *97*(9), 1037–1053. doi: 10.1130/0016-7606(1986)97⟨1037:doowat⟩2.0.co;2

Pleuger, J., & Podladchikov, Y. Y. (2014). A purely structural restoration of the NFP20-East cross section and potential tectonic overpressure in the Adula nappe (central Alps). *Tectonics*, *33*(5), 656–685. doi: 10.1002/2013TC003409

Reuber, G., Kaus, B. J., Schmalholz, S. M., & White, R. W. (2016, may). Non-lithostatic pressure during subduction and collision and the formation of (ultra)high-pressure rocks. *Geology*, *44*(5), 343–346. doi: 10.1130/G37595.1

Ring, U., Brandon, M. T., Willett, S. D., & Lister, G. S. (1999, jan). Exhumation processes. *Geological Society Special Publication*, *154*(1), 1–27. doi: 10.1144/GSL.SP.1999.154.01.01

Rubatto, D., & Hermann, J. (2001, jan). Exhumation as fast as subduction? *Geology*, *29*(1), 3–6. doi: 10.1130/0091-7613(2001)029⟨0003:eafas⟩2.0.co;2

Rubatto, D., Regis, D., Hermann, J., Boston, K., Engi, M., Beltrando, M., & McAlpine, S. R. (2011, may). Yo-yo subduction recorded by accessory minerals in the Italian Western Alps. *Nature Geoscience*, *4*(5), 338–342. doi: 10.1038/ngeo1124

Schenker, F. L., Schmalholz, S. M., Moulas, E., Pleuger, J., Baumgartner, L. P., Podladchikov, Y., . . . Müntener, O. (2015, oct). Current challenges for explaining (ultra)high-pressure tectonism in the Pennine domain of the Central and Western Alps. *Journal of Metamorphic Geology*, *33*(8), 869–886. Retrieved from `http://doi.wiley.com/10.1111/jmg.12143` doi: 10.1111/jmg.12143

Schmalholz, S. M., & Podladchikov, Y. (2014). *Metamorphism under stress: The problem of relating minerals to depth* (Vol. 42) (No. 8). Geological Society of America. doi: 10.1130/focus0822014.1

Schmalholz, S. M., & Podladchikov, Y. Y. (2013, may). Tectonic overpressure in weak crustal-scale shear zones and implications for the exhumation of high-pressure rocks. *Geophysical Research Letters*, *40*(10), 1984–1988. Retrieved from `http://doi.wiley.com/10.1002/grl.50417` doi: 10.1002/grl.50417

Schmalholz, S. M., & Schenker, F. L. (2016, oct). Exhumation of the Dora Maira ultrahigh-pressure unit by buoyant uprise within a low-viscosity mantle oblique-slip shear zone. *Terra Nova*, *28*(5), 348–355. Retrieved from `http://doi.wiley.com/10.1111/ter.12227` doi: 10.1111/ter.12227

Schmid, D. W., & Podladchikov, Y. Y. (2003, oct). Analytical solutions for deformable elliptical inclusions in general shear. *Geophysical Journal International*, *155*(1), 269–288. doi: 10.1046/j.1365-246X.2003.02042.x

Schmid, D. W., & Podladchikov, Y. Y. (2005, mar). Mantled porphyroclast gauges. *Journal of Structural Geology*, *27*(3), 571–585. doi: 10.1016/j.jsg.2004.09.005

Schmid, S. M., Pfiffner, O. A., Froitzheim, N., Schönborn, G., & Kissling, E. (1996, oct). Geophysical-geological transect and tectonic evolution of the Swiss-Italian Alps. *Tectonics*, *15*(5), 1036–1064. doi: 10.1029/96TC00433

Shao, B., & Hou, G. (2019, apr). The interactions of fault patterns and stress fields during active faulting in Central North China Block: Insights from numerical simulations. *PLOS ONE*, *14*(4), e0215893. Retrieved from `https://dx.plos.org/10.1371/journal.pone.0215893` doi: 10.1371/journal.pone.0215893

Tajčmanová, L. (2015, oct). Deviations from lithostatic pressure during metamorphism: fact or fiction? *Journal of Metamorphic Geology*, *33*(8), 783–784. Retrieved from `http://doi.wiley.com/10.1111/jmg.12152` doi: 10.1111/jmg.12152

Tajčmanová, L., Podladchikov, Y., Powell, R., Moulas, E., Vrijmoed, J., & Connolly, J. (2014, feb). Grain-scale pressure variations and chemical equilibrium in high-grade metamorphic rocks. *Journal of Metamorphic Geology*, *32*(2), 195–207. Retrieved from `http://doi.wiley.com/10.1111/jmg.12066` doi: 10.1111/jmg.12066

Tajčmanová, L., Vrijmoed, J., & Moulas, E. (2015, feb). Grain-scale pressure variations in metamorphic rocks: implications for the interpretation of petrographic observations. *Lithos*, *216-217*, 338–351. doi: 10.1016/j.lithos.2015.01.006

Townend, J., & Zoback, M. D. (2000, may). How faulting keeps the crust strong: Comment and Reply. *Geology*, *28*(5), 399–402. doi: 10.1130/0091-7613(2000)28⟨399:HFKTCS⟩2.0.CO

Wang, K., & Hu, Y. (2006). Accretionary prisms in subduction earthquake cycles: The theory of dynamic Coulomb wedge. *Journal of Geophysical Research: Solid Earth*, *111*(6), 1–16. doi: 10.1029/2005JB004094

Warren, C. J. (2013, feb). Exhumation of (ultra-)high-pressure terranes: concepts and mechanisms. *Solid Earth*, *4*(1), 75–92. Retrieved from `https://www.solid-earth.net/4/75/2013/` doi: 10.5194/se-4-75-2013

Wheeler, J. (1991, nov). Structural evolution of a subducted continental sliver: The northern Dora Maira massif, Italian Alps. *Journal of the Geological Society*, *148*(6), 1101–1113. doi: 10.1144/gsjgs.148.6.1101

Wheeler, J. (2014, aug). Dramatic effects of stress on metamorphic reactions. *Geology*, *42*(8), 647–650. doi: 10.1130/G35718.1

Yamato, P., & Brun, J. P. (2017, jan). Metamorphic record of catastrophic pressure drops in subduction zones. *Nature Geoscience*, *10*(1), 46–50. doi: 10.1038/ngeo2852

Yang, J. J., Huang, M. X., Wu, Q. Y., & Zhang, H. R. (2014). Coesite-bearing eclogite breccia: Implication for coseismic ultrahigh-pressure metamorphism and the rate of the process. *Contributions to Mineralogy and Petrology*, *167*(6), 1–17. doi: 10.1007/s00410-014-1013-7